

1 **Insights from elastic thermobarometry into exhumation of high-** 2 **pressure metamorphic rocks from Syros, Greece**

3 Miguel Cisneros^{1,2*}, Jaime D. Barnes¹, Whitney M. Behr^{1,2}, Alissa J. Kotowski^{1,3*}, Daniel F. Stockli¹, and
4 Konstantinos Soukis⁴

5 ¹Department of Geological Sciences, Jackson School of Geosciences, University of Texas at Austin, Austin, TX, USA

6 ^{2*}Current address: Geological Institute, ETH Zürich, Zürich, Switzerland

7 ^{3*}Current address: Department of Earth and Planetary Sciences, McGill, Montreal, Canada

8 ⁴Faculty of Geology and Geoenvironment, NKUA, Athens, Greece

9 *Correspondence to:* Miguel Cisneros (miguel.cisneros@erdw.ethz.ch)

10 **Abstract.** Retrograde metamorphic rocks provide key insights into the pressure-temperature (P-T) evolution of exhumed
11 material, and resultant P-T constraints have direct implications for the mechanical and thermal conditions of subduction
12 interfaces. However, constraining P-T conditions of retrograde metamorphic rocks has historically been challenging and has
13 resulted in debate about the conditions experienced by these rocks. In this work, we combine elastic thermobarometry with
14 oxygen isotope thermometry to quantify the P-T evolution of retrograde metamorphic rocks of the Cycladic Blueschist Unit
15 (CBU), an exhumed subduction complex exposed on Syros, Greece. We employ quartz-in-garnet and quartz-in-epidote
16 barometry to constrain pressures of garnet and epidote growth near peak subduction conditions and during exhumation,
17 respectively. Oxygen isotope thermometry of quartz and calcite within boudin necks was used to estimate temperatures during
18 exhumation and to refine pressure estimates. Three distinct pressure groups are related to different metamorphic events and
19 fabrics: high-pressure garnet growth at ~1.4 - 1.7 GPa between 500 - 550 °C, retrograde epidote growth at ~1.3 - 1.5 GPa
20 between 400 - 500 °C, and a second stage of retrograde epidote growth at ~1.0 GPa and 400 °C. These results are consistent
21 with different stages of deformation inferred from field and microstructural observations, recording prograde subduction to
22 blueschist-eclogite facies and subsequent retrogression under blueschist-greenschist facies conditions. Our new results indicate
23 that the CBU experienced cooling during decompression after reaching maximum high-pressure/low-temperature conditions.
24 These P-T conditions and structural observations are consistent with exhumation and cooling within the subduction channel
25 in proximity to the refrigerating subducting plate, prior to Miocene core-complex formation. This study also illustrates the
26 potential of using elastic thermobarometry in combination with structural and microstructural constraints, to better understand
27 the P-T-deformation conditions of retrograde mineral growth in HP/LT metamorphic terranes.

28 **1 Introduction**

29 Constraining the pressure-temperature (P-T) evolution of metamorphic rocks is fundamental for understanding the
30 mechanics, timescales, and thermal conditions of plate tectonic processes operating on Earth. Historically, one of the most
31 challenging aspects of thermobarometry has been deciphering the P-T evolution of rocks during their exhumation from peak
32 depths back to the surface (e.g., Essene, 1989; Kohn and Spear, 2000; Pattison et al., 2003; Schliestedt and Matthews, 1987;
33 Spear and Pattison, 2017; Spear and Selverstone, 1983). Exhumation P-T paths are particularly challenging to reconstruct
34 because during retrogression rocks are cooled, fluids are consumed by metamorphic reactions, and strain is progressively
35 localized, all of which result in more sluggish reaction kinetics and lesser degrees of chemical equilibrium (e.g., Baxter, 2003;
36 Carlson, 2002; Jamtveit et al., 2016; Rubie, 1998). These issues are especially pronounced in high-pressure/low-temperature
37 (HP/LT) environments characteristic of subduction zones.

38 Elastic thermobarometry offers an alternative to conventional thermobarometry. Rather than relying on equilibrium
39 metamorphic reactions, this approach constrains the P-T conditions at which a host crystal entraps an inclusion (e.g., Adams
40 et al., 1975a, 1975b; Rosenfeld, 1969; Rosenfeld and Chase, 1961). Because inclusion-host-pair bulk moduli and thermal
41 expansivities commonly differ, upon ascent, an inclusion develops residual strain(s) that can be determined from measurements
42 of Raman shifts. A residual inclusion pressure can be calculated from strain(s) by using Grüneisen tensors (Angel et al., 2019;
43 Murri et al., 2018, 2019) or experimental hydrostatic calibrations (e.g., Ashley et al., 2014; Enami et al., 2007; Thomas and
44 Spear, 2018). Elastic modeling is then used to calculate the initial entrapment conditions of when the host grew around the
45 inclusion, and thus can be used to determine the conditions at which individual host minerals grew during metamorphism (e.g.,
46 Alvaro et al., 2020; Ashley et al., 2014; Enami et al., 2007).

47 The purpose of this study is to illustrate the potential of using elastic thermobarometry in combination with structural
48 and microstructural observations, to better understand the P-T-deformation (D) conditions of prograde-to-peak and retrograde
49 mineral growth in subduction-related HP/LT metamorphic rocks. We focus on a subduction complex exposed on Syros Island,
50 Cyclades, Greece, where despite several decades of petrological study, the early exhumation history remains enigmatic. We
51 combine the recently tested quartz-in-epidote (qtz-in-ep) barometer (Cisneros et al., 2020), quartz-in-garnet (qtz-in-grt)
52 barometry (e.g., Ashley et al., 2014; Bonazzi et al., 2019; Thomas and Spear, 2018), and oxygen isotope thermometry (e.g.,
53 Javoy, 1977; Urey, 1947), to constrain metamorphic growth pressures and temperatures near peak subduction depths and
54 during early exhumation. The results demonstrate that combining qtz-in-ep barometry with careful structural and
55 microstructural observations allows us to delineate a retrograde P-T-D path that is contextually constrained, and **provide new**
56 **insights into the exhumation history of the CBU on Syros, Greece.**

57 **2. Geologic Setting**

58 Syros Island in the Cyclades of Greece consists of metamorphosed tectonic slices of oceanic and continental affinity
59 that belong to the Cycladic Blueschist Unit (CBU), structurally below the Pelagonian Upper Unit (Fig. 1). CBU rocks on Syros

60 record Eocene subduction (~52 - 49 Ma) to peak blueschist-eclogite facies conditions (Bröcker et al., 2013; Cliff et al., 2017;
61 Lagos et al., 2007; Laurent et al., 2017; Lister and Forster, 2016; Putlitz et al., 2005; Tomaschek et al., 2003; Uunk et al.,
62 2018), followed by exhumation during Oligo-Miocene (~25 Ma) back-arc extension (e.g., Jolivet and Brun, 2010; Ring et al.,
63 2010). A retrograde regional metamorphic event occurred between 25-18 Ma and caused greenschist- to amphibolite facies
64 metamorphism in the Cycladic islands, but was most pervasive in the footwall adjacent to the large-scale extensional North
65 and West Cycladic Detachment Systems (e.g., Bröcker et al., 1993; Bröcker and Franz, 2006; Gautier et al., 1993; Grasemann
66 et al., 2012; Jolivet et al., 2010; Pe-Piper and Piper, 2002; Schneider et al., 2018). Despite these documented metamorphic
67 events, the exhumation history of the CBU between ~52 and ~25 Ma remains enigmatic and poorly constrained; yet, this period
68 spans exhumation of the CBU from maximum subduction to middle crust pressures (~0.3 - 0.7 GPa). Previous work has
69 constrained some aspects of the early exhumation history of the CBU on Syros, including: the timing of peak and retrograde
70 metamorphism (e.g., Bröcker et al., 2013; Cliff et al., 2017; Lagos et al., 2007; Laurent et al., 2017; Skelton et al., 2018;
71 Tomaschek et al., 2003), prograde and exhumation-related kinematics (e.g., Behr et al., 2018; Keiter et al., 2011; Kotowski
72 and Behr, 2019; Laurent et al., 2016; Philippon et al., 2011; Rosenbaum et al., 2002), and the retrograde P-T path (e.g., Laurent
73 et al., 2018; Ring et al., 2020; Schumacher et al., 2008; Skelton et al., 2018; Trotet et al., 2001a, 2001b); however, debate
74 remains about the relationship between deformation events and retrograde metamorphism, the maximum pressure reached by
75 different CBU rock types, the retrograde P-T path, and the mechanisms and kinematics of CBU exhumation.

76 In this work, we focus on rocks within the CBU, which consist of intercalated metavolcanic and metasedimentary
77 rocks, metabasites, and serpentinites (e.g., Keiter et al., 2011). The CBU has been separated into the “Upper Cycladic
78 Blueschist Nappe” and the “Lower Cycladic Blueschist Nappe” on Milos Island; the Upper Nappe records peak pressure
79 conditions above ~0.8 GPa (~2.0 GPa and 550 °C; Grasemann et al., 2018). **Previous studies have reported a wide range of
80 maximum P-T conditions for rocks from the Upper Cycladic Blueschist Nappe on different Cycladic islands [Sifnos: ~1.4 –
81 2.2 GPa and 450 – 550 °C (e.g., Schmädicke and Will, 2003; Groppo et al., 2009; Dragovic et al., 2012, 2015; Schliestedt and
82 Matthews, 1987; Matthews and Schliestedt, 1984; Ashley et al., 2014; Spear et al., 2006); Tinos: ~1.4 – 2.6 GPa and ~450 –
83 550 °C (e.g., Bröcker et al., 1993; Lamont et al., 2020; Parra et al., 2002); Naxos: ~1.2 – 2.0 GPa and ~450 – 600 °C (e.g.,
84 Avigad, 1998; Peillod et al., 2017, 2021); Sikinos: ~1.1 – 1.7 GPa and ~ 500 °C (e.g., Augier et al., 2015; Gupta and Bickle,
85 2004)].** Some conventional thermobarometry (i.e., thermobarometry techniques that rely on chemical equilibrium) suggests
86 that the CBU on Syros reached peak P-T conditions of ~1.5 GPa and ~500 °C (Ridley, 1984). Trotet et al. (2001a) and Laurent
87 et al. (2018) suggest higher peak P-T conditions of ~2.0 - 2.4 GPa and ~500 - 550 °C; however, multi-mineral phase equilibria
88 of marbles (Schumacher et al., 2008) and elastic thermobarometry of metabasites from Kini beach (Behr et al., 2018) support
89 the original P-T estimates of ~1.5 GPa and 500 °C. Published exhumation P-T paths for the CBU on Syros are also highly
90 variable, ranging from cooling during decompression, near-isothermal decompression, to cooling during decompression
91 followed by reheating at moderate pressures (Laurent et al., 2018; Schumacher et al., 2008; Skelton et al., 2018; Trotet et al.,
92 2001a). Because of these conflicting P-T paths, several models have been proposed to explain the exhumation history of the
93 CBU, including coaxial vertical thinning (Rosenbaum et al., 2002), extrusion wedge tectonics (Keiter et al., 2011; Ring et al.,

94 2020), multiple cycles of thrusting and extension (Lister and Forster, 2016), continuous accretion and syn-orogenic extension
95 (Trotet et al., 2001a, b), and subduction channel exhumation (Laurent et al., 2016).

96 **3. Field and Microstructural Observations**

97 We studied four localities on Syros (Kalamisia, Delfini, Lotos, Megas Gialos; Fig. 1). Each locality exhibits multiple
98 stages of mineral growth, and the same deformation and P-T progression. **The abbreviations D, F, and S refer to deformation,**
99 **folde, and foliations, respectively. Subscripts are listed in alphabetical order to differentiate older and younger stages of**
100 **deformation (i.e., D_s, D_t). D_s is the oldest observed deformation in outcrop that is recorded by tight isoclinal folds (F_s) that**
101 **define the primary foliation (S_s). D_t refers to younger deformation that is defined by upright folds (F_t). We assign subscripts**
102 **in numerical order to indicate older (D_{t1}) and younger (D_{t2}) upright folding.** Kalamisia records blueschist facies metamorphism,
103 and Delfini, Lotos, and Megas Gialos record blueschist-greenschist facies metamorphism. GPS coordinates of collected
104 samples and their associated mineralogy are provided in the supplementary material (Supplementary Table S1). 1 – 4 samples
105 from each locality were examined petrographically.

106 **3.1 Kalamisia**

107 Mafic rocks from Kalamisia preserve retrograde blueschist facies metamorphism (Fig. 1). Protoliths of Kalamisia
108 rocks are fine-grained basalts. They exhibit an early foliation (S_s) characterized by relict blueschist and eclogite facies minerals.
109 The early S_s fabric is re-folded by upright folds (F_{t1}) with steeply dipping axial planes, NE-SW-oriented fold hinge lines, and
110 NE-SW-oriented stretching lineations primarily defined by white mica, glaucophane, and epidote; this indicates syn-blueschist
111 facies folding (D_{t1}).

112 Garnets in Kalamisia mafic samples occur as ~1 - 4 mm porphyroblasts (KCS70A, Supplementary Fig. S1), lack a
113 well-defined internal foliation, and the S_s foliation deflect around garnets. Glaucophane typically grows within pressure
114 shadows and brittle fractures of garnet, and omphacite displays breakdown and alteration to glaucophane; this indicates
115 retrograde glaucophane growth. Glaucophane inclusions within epidote are commonly oriented parallel to S_s, and no omphacite
116 is observed as inclusions within epidote; these observations support epidote (ep1) growth during retrograde metamorphism.

117 **3.2 Delfini Beach**

118 Metasedimentary rocks (quartz-rich lenses intermixed with metavolcanics) at Delfini Beach show retrogression from
119 eclogite- and blueschist- to greenschist facies (Fig. 1). Protoliths of Delfini rocks remain enigmatic, but may be graywackes
120 or sandstones variably intermixed with mafic tuffitic intercalations. The rocks at Delfini exhibit an early foliation (also
121 considered S_s) characterized by relict blueschist and eclogite facies minerals (garnet porphyroblasts, and foliation-parallel
122 white mica, blue amphibole, and epidote) aligned in tight isoclinal folds (F_s) with shallow axial planes. This early fabric was
123 locally retrogressed and re-folded by upright folds (considered F_{t2}) with steeply dipping axial planes, E-W-oriented fold hinge

124 lines, and E-W-oriented stretching lineations primarily defined by white mica, chlorite, and actinolite (considered D_{t2} , Fig.
125 2a,b); this indicates folding under greenschist facies conditions. D_{t2} folding was associated with boudinage of earlier-
126 generation epidote parallel to the fold hinge lines, and simultaneous precipitation of new coarse-grained epidote (ep2), along
127 with quartz, calcite and iron oxides in boudin necks (Fig. 3). In some areas of tight D_{t2} folding, a new generation of fine-
128 grained epidote (also interpreted as ep2) grows within a newly developed crenulation cleavage (S_{t2} , Fig. 2c,d,e).

129 Garnets in Delfini metasedimentary samples occur as ~1 - 4 mm, partially chloritized porphyroblasts (KCS34, Fig.
130 2c), and as <1 mm garnets that are commonly found as inclusions within epidote (KCS1621, Supplementary Fig. S3). Foliation
131 parallel epidotes (ep1) found within early blueschist-greenschist facies outcrops (KCS1621) range in size from ~0.5 – 5 mm
132 (b-axis length), are strongly poikiloblastic, lack late greenschist facies inclusions such as chlorite, and commonly contain an
133 internal foliation that is oblique to the external matrix S_s foliation (Fig. 2f,g; Supplementary Fig. S3). Late epidote (ep2)
134 crystals are found within sample KCS34 from the core of an upright fold (F_{t2}). During upright folding, a predominant portion
135 of the rock is recrystallized to late-stage greenschist facies minerals, and contains new epidote (ep2) that is oriented parallel to
136 the S_{t2} crenulation cleavage. Ep2 crystals range from ~50 - 300 μm along the b-axis (Fig. 2c,d,e), tend to be euhedral (Fig.
137 2d,e), sometimes contain titanite inclusions (Fig. 2d), and show textural equilibrium with white mica and titanite that also
138 formed in the S_{t2} cleavage (Fig. 2d,e). Ep2 crystals are not poikiloblastic and rarely preserve quartz inclusions, thus only a few
139 analyses were possible.

140 **3.3 Lotos Beach**

141 The rocks from Lotos Beach exhibit the same structural and petrological progression as those from Delfini (Fig. 1),
142 showing retrogression from eclogite- and blueschist- to greenschist facies. Protoliths of Lotos rocks are primarily fine-grained
143 volcanics. An early S_s foliation was locally retrogressed and re-folded by upright F_{t2} folds with steeply dipping axial planes,
144 E-W-oriented fold hinge lines, and E-W-oriented stretching lineations primarily defined by white mica, chlorite, and actinolite
145 (D_{t2}). D_{t2} folding was associated with boudinage of earlier-generation epidote parallel to the fold hinge lines, and simultaneous
146 precipitation of new coarse-grained epidote (ep2), along with quartz, calcite and iron oxides in boudin necks (Fig. 3).

147 Garnets in Lotos samples occur as ~1 - 3 mm chloritized porphyroblasts (e.g., KCS3), that deflect the external S_s
148 foliation (KCS3). Foliation parallel epidotes (ep1) found within early blueschist-greenschist facies outcrops (SY1402, SY1405,
149 KCS2, KCS3) range in size from ~0.5 – 5 mm (b-axis length), are strongly poikiloblastic, and commonly contain an internal
150 foliation that is oblique to the external matrix S_s foliation (Supplementary Fig. S4). Boudinage of ep1 parallel to stretching
151 lineations is common in thin sections (Supplementary Fig. S4).

152 **3.4 Megas Gialos**

153 The rocks from Megas Gialos exhibit the same structural and petrological progression as those from Lotos and Delfini
154 Beaches (Fig. 1). Protoliths of Megas Gialos rocks remain enigmatic, but may be sediments intermixed with volcanics. Rocks

155 from Megas Gialos show retrogression from eclogite- and blueschist- to greenschist facies. An early S_s foliation was locally
156 retrogressed and stretching lineations primarily defined by white mica, chlorite, and actinolite are E-W-oriented.

157 No garnets were found within the analyzed sample from Megas Gialos. Foliation parallel epidotes (ep1) found within
158 early blueschist-greenschist facies outcrops range in size from $\sim 0.5 - 3$ mm (b-axis length), are strongly poikiloblastic, and
159 commonly contain an internal foliation that is oblique to the external matrix S_s foliation (Supplementary Fig. S5). Boudinage
160 of ep1 parallel to stretching lineations is common in thin sections (Supplementary Fig. S5).

161 4. Methods

162 We determined P-T conditions using elastic thermobarometry and oxygen isotope thermometry. Raman spectroscopy
163 was used to measure Raman shifts of strained quartz inclusions entrapped within epidote or garnet, and a laser fluorination
164 line and a GasBench II coupled to a gas source mass spectrometer was used to measure oxygen isotope ratios of quartz and
165 calcite separates, respectively.

166 4.1 Raman Spectroscopy measurements

167 Our Raman spectroscopy measurements are taken from ~ 30 μm , ~ 80 μm , and ~ 150 μm thin and thick sections, that
168 consist of sections cut perpendicular to foliation (S_s) and parallel to stretching lineations (e.g., KCS1621), and perpendicular
169 to the F_2 fold axial plane (KCS34). Quartz inclusions were measured from multiple epidotes and garnets within individual
170 sections (Supplementary Table S3). Measured quartz inclusions were small in diameter relative to the host, and were two-to-
171 three-times the inclusion radial distance from other inclusions, fractures, and the host exterior to avoid overpressures or stress
172 relaxation (Fig. 4a,b; Campomenosi et al., 2018; Zhong et al., 2020). No geometric corrections were applied (Mazzucchelli et
173 al., 2018).

174 Raman spectroscopy measurements of quartz inclusions within garnet and epidote were carried-out at Virginia Tech
175 (VT) and ETH Zürich (ETHZ) by using JY Horiba LabRam HR800 and DILOR Labram Raman systems, respectively.
176 Analyses at VT used an 1800 grooves mm^{-1} grating, 100x objective with a 0.9 numerical aperture (NA), 400 μm confocal
177 aperture, and a 150 μm slit width. Raman spectra were centered at ~ 360 cm^{-1} . We used a 514.57 nm wavelength Ar laser, and
178 removed the laser interference filter for all analyses to apply a linear drift correction dependent on the position of the 116.04
179 cm^{-1} , 266.29 cm^{-1} , and 520.30 cm^{-1} Ar plasma lines (Fig. DR4). Measurements at ETHZ used a 532 nm laser, an 1800 grooves
180 mm^{-1} grating, a 100x objective with a 0.9 NA, a 200 μm confocal aperture, and a 300 μm slit width. Raman spectra were
181 centered at ~ 850 cm^{-1} .

182 All Raman spectra was reduced with a Bose-Einstein temperature-dependent population factor (Kuzmany, 2009). All
183 Raman bands were fit by using PeakFit v4.12 from SYSTAT Software Inc. A Gaussian model was used to fit Ar plasma lines
184 (only VT analyses), and a Voigt model was used to fit the quartz 128 cm^{-1} , 206 cm^{-1} , and 464 cm^{-1} bands, epidote bands, and
185 garnet bands. Raman bands of quartz, epidote, and garnet, and Ar plasma lines were fit simultaneously, and a linear background

186 subtraction was applied during peak fitting. Baseline-to-baseline deconvolution of quartz and garnet bands was simple and
187 generally required fitting quartz bands and a few shoulder garnet bands. Deconvolution of quartz and epidote bands required
188 more complicated deconvolution; we followed a fitting approach similar to that described by Cisneros et al. (2020).

189 **4.2 Inclusion and entrapment pressure calculations**

190 The fully encapsulated inclusions preserve strain that causes the Raman active vibrational modes of inclusions to be
191 shifted to higher or lower wavenumbers relative to minerals that are unstrained (fully exposed). We calculated the Raman
192 shift(s) of inclusions (ω_{inc}) relative to Raman shift(s) of an unencapsulated Herkimer quartz standard (ω_{ref}) at ambient
193 conditions ($\Delta\omega = \omega_{\text{inc}} - \omega_{\text{ref}}$) (Fig. 4). For VT analyses, ω_{inc} was measured relative to a Herkimer quartz standard that was
194 analyzed 5 times prior to same day analyses. A drift correction was applied to ω_{inc} by monitoring the position of Ar plasma
195 lines (Supplementary Tables S2; S3). For ETHZ analyses, a Herkimer quartz standard was analyzed 3 times prior to and after
196 quartz inclusion analyses. A time-dependent linear drift correction was applied to ω_{inc} based on the drift shown by Herkimer
197 quartz analyses that bracketed inclusion analyses ($< 0.2 \text{ cm}^{-1}$).

198 We calculated residual inclusion pressures (P_{inc}) by using hydrostatic calibrations and by accounting for quartz
199 anisotropy. To calculate a P_{inc} from individual quartz Raman bands, we used pressure-dependent Raman shift(s) ($P\text{-}\Delta\omega$) of the
200 quartz 128 cm^{-1} , 206 cm^{-1} , and 464 cm^{-1} bands, that have been experimentally calibrated under hydrostatic stress conditions
201 by using diamond anvil cell experiments (Schmidt and Ziemann, 2000). To account for quartz anisotropy, we calculated P_{inc}
202 from strains. Calculating quartz strains requires that the Raman shift of at least 2 quartz vibrational modes can be measured.
203 When we were able to measure the quartz 128 , 206 and 464 cm^{-1} band positions of inclusions, we calculated strains from the
204 $\Delta\omega$ of 3 bands. If only two bands were measured, we calculated strains from the $\Delta\omega$ of 2 bands (Supplementary Table S3). For
205 the remaining analyses with low 128 and 206 cm^{-1} intensities, we report P_{inc} calculated from the 464 cm^{-1} band hydrostatic $P\text{-}$
206 $\Delta\omega$ relationship (Supplementary Table S3). Strains were determined from the $\Delta\omega$ of the 128 cm^{-1} , 206 cm^{-1} , and 464 cm^{-1}
207 quartz bands by using Strainman (Angel et al., 2019; Murri et al., 2018, 2019), wherein a weighted fit was applied based on
208 the $\Delta\omega$ error associated with each quartz Raman band. Calculated strains were converted to a mean stress [$P_{\text{inc}} = (2\sigma_1 + \sigma_3)/3$]
209 using the matrix relationship $\sigma_i = c_{ij}\epsilon_j$, where σ_i , c_{ij} , and ϵ_j , are the stress, elastic modulus, and strain matrices, respectively. We
210 used the α -quartz trigonal symmetry constraints of Nye (1985) and quartz elastic constants of Wang et al. (2015).

211 We assumed constant mineral compositions for all modeling (epidote: $X_{\text{ep}} = 0.5$ and $X_{\text{cz}} = 0.5$; garnet: $X_{\text{Alm}} = 0.7$,
212 $X_{\text{Gr}} = 0.2$, and $X_{\text{Py}} = 0.1$). Garnet compositions have a negligible effect on entrapment pressures (P_{trap}) because the
213 thermodynamic and physical properties of garnet end-members are similar (e.g., Supplementary Table S8). Epidote
214 composition has a greater effect on P_{trap} , but the compositional dependence is minor $< 1.5 \text{ GPa}$ (Cisneros et al., 2020). To
215 account for epidote and garnet solid solutions, we implemented linear mixing of shear moduli and molar volumes (V). Ideal
216 mixing of molar volumes has been shown to be an appropriate approximation for epidote-clinozoisite solid solutions (Cisneros
217 et al., 2020; Franz and Liebscher, 2004). Garnet molar volumes were modeled using the thermodynamic properties of Holland
218 and Powell (2011) (almandine and pyrope) and Milani et al. (2017) (grossular), and a Tait Equation of State (EoS) with a

219 thermal pressure term. We used the shear moduli of Wang and Ji (2001) (almandine and pyrope) and Isaak et al. (1992)
220 (grossular). Epidote molar volumes were modeled using the thermodynamic properties and shear moduli given by Cisneros et
221 al. (2020), and a Tait EoS and thermal pressure term. Epidote and clinozoisite regressions are based on the P-V-T data of Gatta
222 et al. (2011) ($X_{ep} = 0.74$), and T-V and P-V data of Pawley et al. (1996) ($X_{ep} = 0$) and Qin et al. (2016) ($X_{ep} = 0.39$), respectively.
223 Clinozoisite and epidote have similar thermal expansivities but differing bulk moduli (Supplementary Table S4). To account
224 for the composition of epidotes used in P-V-T experiments, we normalized the composition of our unknown epidotes across
225 the compositional range of P-V experimental epidotes, i.e., the molar volume of our unknown epidote ($X_{ep} = 0.5$) is estimated
226 as 31 % ($X_{ep} = 0.74$) and 69 % ($X_{ep} = 0.39$) of each experimental epidote. Quartz molar volumes were modeled using the
227 thermodynamic properties and approach of Angel et al. (2017a). Entrapment pressures were calculated from residual quartz
228 P_{inc} by using the Angel et al. (2017b) 1D elastic model equation, and a MATLAB program available in Cisneros and Befus
229 (2020) that implements mixing of shear moduli and molar volumes. A comparison of entrapment pressures calculated from
230 the Cisneros and Befus (2020) MATLAB program and EoSFit-Pinc (Angel et al., 2017b) is given in Supplementary Table S4;
231 entrapment pressure calculations of mineral end-members accounts for the reproducibility of molar volume and elastic
232 modeling calculations.

233 **4.3 Stable isotope measurements**

234 Samples were measured by using a ThermoElectron MAT 253 isotope ratio mass spectrometer (IRMS) at the
235 University of Texas at Austin. Quartz $\delta^{18}O$ values were measured by laser fluorination (Sharp, 1990), and ~2.0 mg of quartz
236 were used in each analysis. Quartz from samples SY1613, SY1617, and SY1623 was duplicated to determine isotopic
237 homogeneity and reproducibility. An internal quartz Lausanne-1 standard ($\delta^{18}O = +18.1\text{‰}$) was analyzed with all samples to
238 evaluate precision and accuracy. All $\delta^{18}O$ values are reported relative to standard mean ocean water (SMOW), where the $\delta^{18}O$
239 value of NBS-28 is +9.65‰. Measurement precision based on the long-term reproducibility of standards is $\pm 0.1 \text{‰}$ (1 σ).
240 Precision of Lausanne-1 on the day of analysis was $\pm 0.3 \text{‰}$ (1 σ), whereas samples reproduced with a precision of $\pm 0.1 \text{‰}$
241 (1 σ) or better (Supplementary Table S5). Calcite $\delta^{18}O$ values were measured on a Thermo Gasbench II coupled to a
242 ThermoElectron 253 mass spectrometer. Each analysis used 0.25 - 0.5 mg of calcite that was loaded into Exetainer vials,
243 flushed with ultra-high purity helium, and reacted with 103 % phosphoric acid at 50 °C for ~2 hours. Headspace CO₂ was then
244 transferred to the mass spectrometer. Samples were calibrated to an in-house standard, NBS-18, and NBS-19. Measurement
245 precision is $\pm 0.04 \text{‰}$ (1 σ) based on the long-term reproducibility of standards.

246 **4.4 Stable isotope temperature calculations**

247 Temperatures derived from stable isotope measurements were calculated by using the Sharp and Kirschner (1994)
248 quartz-calcite oxygen isotope fractionation calibration ($A = 0.87 \pm 0.06$; equation A1; Supplementary Table S5). Isotopic
249 equilibrium was assumed for all samples. Several observations support that this assumption is appropriate: 1) duplicate $\delta^{18}O$

250 analysis of quartz and calcite grains give the same isotopic value, suggesting grain isotopic homogeneity, 2) the stage of
251 deformation that these mineral pairs are related to is not affected by further deformation in either outcrop or thin section, and
252 3) all quartz-calcite pairs suggest a similar temperature of isotopic equilibration.

253 Temperature errors from quartz-calcite oxygen isotope measurements were calculated through the square-root of the
254 summed quadratures of all sources of uncertainty (equations A2, A3). These uncertainties included $\delta^{18}\text{O}$ value errors of quartz
255 and calcite of $\pm 0.1 \text{ ‰}$ (1σ) and $\pm 0.04 \text{ ‰}$ (1σ), respectively, and errors associated with the Sharp and Kirschner (1994)
256 quartz-calcite oxygen isotope fractionation calibration (A parameter).

257 **4.5 Electron probe measurements**

258 Electron probe analyses were carried-out at ETHZ using a JEOL JXA-8230 Electron Probe Microanalyzer (EPMA).
259 The EPMA is equipped with five wavelength-dispersive spectrometers. Epidote and pyroxene were analyzed for Si, Al, Na,
260 Mg, Ca, Cr, K, Ti, Fe, and Mn on TAP (Si, Al), TAPH (Al, Ca), PETJ (Ca, Cr), PETL (K, Ti), and LIFH (Fe, Mn) crystals.
261 Beam parameters included a 20 nA beam current, 10 μm beam size, and a 15 keV accelerating voltage. All elements were
262 measured for 30 s on peak and a mean atomic number background correction was applied. Primary calibration standards used
263 included: albite (Si, Na), anorthite (Al, Ca), synthetic forsterite (Mg), chromite (Cr), microcline (K), synthetic rutile (Ti),
264 synthetic fayalite (Fe), and synthetic pyrolusite (Mn). Mole fraction expressions from Franz and Liebscher (2004) were used
265 to calculate epidote (X_{ep}), clinozoisite (X_{cz}), and tawmawite (X_{taw}) compositions. Further information on mineral chemistry
266 calculations is available in Supplementary Table S6. Garnets were analyzed for Al, Ca, Mn, Fe, Mg on TAP (Al), PETJ (Ca),
267 LIFL (Mn), LIFH (Fe), and TAPH (Mg) crystals. Si was calculated stoichiometrically. X-ray maps were collected with a 50
268 nA beam current, 15 keV accelerating voltage, 100 ms dwell time, and 5 μm (KCS34 Garnet 1) and 4 μm (KCS34 Garnet 3)
269 step sizes. X-ray maps were reduced using CalcImage (Probe for EPMA).

270 **5. Thermobarometry Results**

271 Determined pressures were categorized into three groups according to outcrop and microstructural context (Fig. 5;
272 Fig. 7; Supplementary Table S3): garnet growth near peak metamorphic conditions (Group 1), growth of foliation-parallel
273 epidote during blueschist-greenschist facies metamorphism (ep1, Group 2), and late-stage epidote growth in the new
274 crenulation (S_{12}) associated with F_{12} folds during greenschist facies metamorphism (ep2, Group 3). New ep2 growth is also
275 supported by the mineral chemistry of different epidote generations within the S_{12} crenulation. Epidotes show a progressive
276 chemical evolution that is recorded by an early generation epidote inclusion in titanite that occurs parallel to S_{12} ($X_{\text{ep}} \cong 0.1$),
277 the ep2 core ($X_{\text{ep}} \cong 0.5$), and the ep2 rim ($X_{\text{ep}} \cong 0.8$) (Fig. 2g; Supplementary Table S6).

278 The entrapment temperature (T_{trap}) of quartz inclusions in garnet (garnet growth temperature) is estimated as 500 -
279 550 $^{\circ}\text{C}$; this is based on good agreement between previous studies on the maximum temperature reached by CBU rocks from
280 Syros (e.g., Laurent et al., 2018; Ridley, 1984; Schumacher et al., 2008; Skelton et al., 2018; Trotet et al., 2001a). T_{trap} for the

281 ep2 population (Group 3) is deduced from oxygen isotope thermometry of quartz-calcite boudin-neck precipitates. The mean
282 temperature from quartz-calcite pairs from boundin necks is 411 ± 23 °C (n = 4, Supplementary Table S5). T_{trap} for the ep1
283 population (Group 2) is estimated as being intermediate between garnet and ep2 growth (~400 - 500 °C). As shown by qtz-in-
284 ep isomekes (constant P_{inc} lines along which fractional volume changes of an inclusion and host are equal), the assumed T_{trap}
285 has a minimal effect on P_{trap} (Fig. 7a; Cisneros et al., 2020).

286 **5.1 Kalamisia**

287 Group 1 quartz-inclusions-in-garnet record a mean P_{inc} of 600 ± 78 MPa (Fig. 5; Supplementary Table S3). This
288 corresponds to an entrapment pressure (P_{trap}) of 1.43 - 1.49 ± 0.14 GPa (n = 5), at an estimated T_{trap} between 500 - 550 °C (Fig.
289 7a, Supplementary Table S3). Group 2 quartz-inclusions-in-ep1 record a mean P_{inc} of 544 ± 57 MPa, corresponding to a P_{trap}
290 of 1.43 ± 0.12 GPa (n = 6) at an estimated T_{trap} of 450 °C. No Group 3 epidotes are found within our analyzed section from
291 Kalamisia.

292 **5.2 Delfini**

293 Group 1 records a mean P_{inc} of 731 ± 54 MPa (Fig 5; Supplementary Table S3). This corresponds to a P_{trap} of 1.66 -
294 1.72 ± 0.10 GPa (n = 22), at an estimated T_{trap} between 500 - 550 °C (Fig. 7a, Supplementary Table S3). Group 2 records a
295 mean P_{inc} of 518 ± 52 MPa, corresponding to a P_{trap} of 1.38 ± 0.11 (n = 5) at an estimated T_{trap} of 450 °C. Group 3 records a
296 mean P_{inc} of 343 ± 23 MPa, corresponding to a P_{trap} of 0.98 ± 0.05 GPa (n = 3) at 411 °C (Supplementary Table S3).

297 **5.3 Lotos**

298 Group 1 records a mean P_{inc} of 751 ± 76 MPa (Fig 5; Supplementary Table S3). This corresponds to a P_{trap} of 1.70 -
299 1.76 ± 0.14 GPa (n = 2), at an estimated T_{trap} between 500 - 550 °C (Fig. 7a; Supplementary Table S3). Group 2 records a mean
300 P_{inc} of 531 ± 78 MPa, corresponding to a P_{trap} of 1.41 ± 0.17 (n = 15) at an estimated T_{trap} of 450 °C. No Group 3 epidotes were
301 analyzed from Lotos.

302 **5.4 Megas Gialos**

303 Group 2 records an average P_{inc} of 494 ± 29 MPa (Fig. 5), corresponding to a P_{trap} of 1.33 ± 0.03 (n = 6) at an estimated
304 T_{trap} of 450 °C (Fig. 7a; Supplementary Table S3). No Group 1 garnets or Group 3 epidotes were analyzed from Megas Gialos.

305 6. Discussion

306 6.1 Elastic thermobarometry pressure groups

307 Group 1 garnets either lack an internal foliation or contain a weak foliation that is defined by inclusions oblique to
308 the S_s fabric, which indicates a previous stage of deformation (Fig. 2c; Supplementary Figs. S1, S2, S3). Garnets record similar
309 pressures, regardless of the location of quartz inclusions (Fig. 6, Supplementary Table S3). Pyroxene inclusions within different
310 garnet zones (core: $X_{jd} \approx 0.84$, rim: $X_{jd} \approx 0.81$) also show no difference in composition, which is consistent with qtz-in-grt
311 barometry results (Delfini: KCS1621, Supplementary Table S6). Group 2 epidotes (ep1) overgrow garnets, are aligned parallel
312 to the S_s foliation but sometimes preserve an internal foliation that is oblique to S_s , and lack late greenschist facies inclusions
313 (Fig. 2f,g; Supplementary Figs. S1, S3, S4, S5). Group 3 epidotes (ep2, KCS34, Fig. 2c, d, e) are short in length, are aligned
314 parallel to a late S_{t2} crenulation, contain minimal quartz inclusions, and only record Group 3 pressures, independent of the
315 position of quartz inclusions within epidotes.

316 Based on these observations, the Group 1 P_{trap} estimates from the qtz-in-grt barometer record high-P conditions on
317 Syros associated with prograde-to-peak garnet growth, and the Group 2 and 3 P_{trap} estimates from the qtz-in-ep barometer
318 record epidote growth during early blueschist-greenschist facies retrogression (ep1, D_{t1}) and subsequent D_{t2} deformation (ep2),
319 respectively. We interpret the low-P epidote group (Group 3) to be associated with D_{t2} folding, and best recorded in areas that
320 experienced late greenschist facies mineral growth due to enhanced deformation and/or fluid influx during this stage of
321 deformation (e.g., core of F_{t2} fold).

322 6.2 Comparison of peak pressure constraints for the CBU on Syros and Sifnos

323 Based on qtz-in-grt measurements (Group 1), our P_{trap} calculations suggest maximum P conditions of ~1.6 - 1.8 GPa
324 were reached by the CBU on Syros. Garnets from metasedimentary and metavolcanic rocks record the statistically highest P_{trap}
325 (~1.5 - 1.8 GPa), whereas garnets from metamafic rocks (Kalamisia) record the lowest P_{trap} (~1.3 - 1.6 GPa) (Fig. 7a). **Several**
326 **observations support that the qtz-in-grt barometry results record max P conditions of the CBU on Syros: 1) quartz inclusion**
327 **measurements across core-to-rims of garnets that show prograde growth (decreasing Mn), show no systematic change in P_{trap}**
328 **(Fig. 6), 2) max pressures from this study are equivalent to qtz-in-grt barometry results from prograde-to-peak eclogites and**
329 **blueschists (non-retrogressed) from the CBU on Syros (Behr et al., 2018), 3) retrograde ep1 pressures, do not exceed those**
330 **recorded by qtz-in-grt barometry, and 4) several studies from the CBU have used garnets to constrain max pressures, suggesting**
331 **that garnets are suitable for constraining maximum pressures (e.g., Laurent et al., 2018; Dragovic et al., 2012, 2015; Groppo**
332 **et al., 2009). We herein discuss our qtz-in-grt barometry results as max pressures constraints, but acknowledge that we may**
333 **have missed high-P rims that have been found in other studies from the CBU on Syros (e.g., Laurent et al., 2018). We present**
334 **a compilation of previous P-T constraints on CBU rocks from Syros and Sifnos, Greece, and discuss how our P_{trap} constraints**
335 **compare with previous studies.**

336 Elastic thermobarometry, mineral stability constraints, and multi-phase equilibrium modeling results from Sifnos
337 CBU rocks suggest maximum P conditions of $\sim 1.8 \pm 0.1$ GPa (Ashley et al., 2014), $\sim 1.4 \pm 0.2$ GPa (Matthews and Schliestedt,
338 1984), and $\sim 2.0 - 2.2$ GPa (Dragovic et al., 2012, 2015; Groppo et al., 2009; Trotet et al., 2001a), respectively. **Elastic**
339 **thermobarometry (Ashley et al., 2014) and garnet modelling results (Dragovic et al., 2012, 2015; Groppo et al., 2009) from**
340 **Sifnos, suggest near isobaric conditions during garnet growth.** The results of Ashley et al. (2014) are commonly cited as
341 evidence that the CBU reached high pressure conditions (≥ 2.0 GPa, from elastic thermobarometry); however, their P_{trap}
342 calculations were carried out by using fits to quartz molar volume (P-T-V) data that have recently been re-evaluated (Angel et
343 al., 2017a). Improved fits to quartz molar volume experiments “soften” quartz, and remodeling P_{inc} values from Ashley et al.
344 (2014) reduces maximum mean P_{trap} conditions to $\sim 1.6 \pm 0.1$ GPa (Fig. 7b, Supplementary Table S7).

345 Elastic thermobarometry, mineral stability constraints, glaucophane-bearing marble mineral equilibria, and multi-
346 phase equilibria modeling results from Syros CBU rocks suggest peak pressure conditions of $\sim 1.5 \pm 0.1$ GPa (Behr et al.,
347 2018), $\sim 1.4 - 1.9$ GPa (Ridley, 1984), ~ 1.5 GPa (Schumacher et al., 2008), and $\sim 1.9 - 2.4$ GPa (Laurent et al., 2018; Skelton
348 et al., 2018; Trotet et al., 2001a), respectively. Elastic thermobarometry results from **prograde-to-peak eclogites and blueschists**
349 **from** Syros, Greece were reduced using the approach outlined in Ashley et al. (2016), wherein a correction to P_{trap} is applied
350 based on the assumed T_{trap} . Recent studies suggest that not using a temperature-dependent P_{trap} correction produces suitable
351 results that accurately reproduce experimental conditions of quartz entrapment by garnet (Bonazzi et al., 2019; Thomas and
352 Spear, 2018). Recalculation of the Behr et al. (2018) P_{inc} data (no temperature-dependent P_{trap} correction) results in a mean P_{trap}
353 of $\sim 1.7 \pm 0.1$ GPa (Fig. 7b, Supplementary Table S8). The re-evaluation of data from Ashley et al. (2014) and Behr et al.
354 (2018) suggests that our results are in good agreement with previous elastic thermobarometry constraints, and that to date, no
355 qtz-in-grt elastic thermobarometry results suggest pressures ≥ 2.0 GPa.

356 Different methodologies applied to CBU rocks from Syros have resulted in a wide range of maximum P estimates.
357 Schumacher et al. (2008) used mineral-equilibria modeling of glaucophane-bearing marbles to place constraints on maximum
358 P-T conditions. Maximum P-T conditions are constrained by the presence of glaucophane + CaCO₃ + dolomite + quartz,
359 which suggests that the marbles exceeded the albite/Na-pyroxene + dolomite + quartz \rightarrow glaucophane + CaCO₃ reaction, but
360 did not cross the dolomite + quartz \rightarrow tremolite + CaCO₃ or the glaucophane + aragonite-out reactions. The mineral reaction
361 constraints suggest maximum P-T conditions of $\sim 1.5 - 1.6$ GPa and 500 °C for the CBU marbles. Ridley (1984) used the
362 stability of paragonite and lack of kyanite to deduce max P constraints of $\sim 1.4 - 1.9$ GPa. Trotet et al. (2001b, 2001a), Laurent
363 et al. (2018), and Skelton et al. (2018) employed thermodynamic phase-equilibria modeling and supplementary methods to
364 constrain P-T conditions for CBU rocks from Syros. Skelton et al. (2018) used the Powell and Holland (1994) Thermocalc
365 database, Trotet et al. (2001b, 2001a) used the Berman (1991) thermodynamic database and the TWEEQC approach, and
366 Laurent et al. (2018) used empirical thermobarometry, GrtMod (Lanari et al., 2017), and isochemical phase diagrams. Trotet
367 et al. (2001b, 2001a), Laurent et al. (2018), and Skelton et al. (2018) found high-P conditions for the CBU (≥ 1.9 GPa), and
368 results from Laurent et al. (2018) suggest some rocks reached conditions as high as 2.2 ± 0.2 GPa. Results from Laurent et al.
369 (2018) suggest most garnet growth occurred at ~ 1.7 GPa and 450 ± 50 °C; however, some garnet modeling results suggest that

370 garnet rims grew at ~2.4 GPa and 500 - 550 °C, albeit errors are increasingly large for these results ($\pm 0.4 - 0.9$ GPa). These
371 errors reflect the spacing between garnet isopleths (optimal P-T conditions), that result from uncertainties in chemical analyses.

372 Some GrtMod results suggest prograde core and rim garnet growth at ~1.8 GPa and 475 °C, and ~2.4 GPa and 475
373 °C, respectively (sample SY1418 from; Laurent et al., 2018); however, the optimal P-T conditions for garnet rims have large
374 errors and plot within uncertainty of garnet core conditions. Garnet results from another sample (SY1401) suggest core and
375 rim garnet growth at ~1.8 GPa and 475 °C, and ~2.4 GPa and 550 °C, respectively. Sample SY1401 is collected from the same
376 locality as ours (Kalamisia), but our qtz-in-grt results from this study suggest that garnets from this outcrop record the
377 statistically lowest P_{trap} . It is possible, however, that we did not sample the same rocks as Laurent et al. (2018), or that we have
378 not found or analyzed garnets that record high pressures.

379 Previous studies have also suggested that pressures ≥ 2.0 GPa are unreasonable for Syros because paragonite is
380 abundant in CBU rocks, but kyanite has not been reported. This suggests that CBU rocks did not cross the reaction paragonite
381 \rightarrow jadeite₅₀ + kyanite + H₂O (~1.9 - 2.0 GPa); however, we recognize that the occurrence of kyanite may require high
382 Al₂O₃:SiO₂ ratios for metabasites (e.g., Liati and Seidel, 1996), and that the pressure of this reaction is compositionally
383 dependent. Pseudosections of eclogite CBU rocks show that kyanite would not be found in these bulk compositions below
384 ~2.3 GPa (Skelton et al., 2018). It is possible that the high-P conditions found in previous studies may be real, but may only
385 be recorded locally within some eclogite blocks.

386 In general, phase stability relationships (e.g., Matthews and Schliestedt, 1984; Ridley, 1984; Schumacher et al., 2008)
387 and qtz-in-grt barometry results are in good agreement, but do not agree with high-pressure results (≥ 1.9 GPa) deduced from
388 thermodynamic modeling using approaches such as GrtMod and TWEEQC. The difference between our results and those of
389 previous studies is important to reconcile, because the maximum P conditions reached by the CBU has considerable
390 implications for the internal architecture of the CBU, its geodynamic evolution, and the mechanisms that can accommodate
391 exhumation mechanisms of high-P subduction zone rocks from Syros. A comparison of qtz-in-grt barometry with
392 thermodynamic modeling results from samples that record high pressures would be appropriate for further testing differences
393 between the two techniques.

394 **6.3 Comparison of exhumation P-T conditions**

395 Previous studies have presented varying P-T paths and associated exhumation histories for Syros CBU rocks (Fig.
396 7a; Laurent et al., 2018; Schumacher et al., 2008; Skelton et al., 2018; Trotet et al., 2001a). We present a compilation of
397 previous P-T constraints and interpretations and discuss how our results compare with previous studies.

398 Schumacher et al. (2008) do not provide quantitative constraints for the retrograde P-T path (schematic), and samples
399 do not have structural context; however, the authors suggest that a “cold” P-T path during exhumation is required for Syros
400 CBU rocks based on the occurrence of lawsonite + epidote assemblages across Syros, and the P-T path required to avoid
401 crossing the lawsonite \rightarrow kyanite + zoisite reaction (Fig. 7b). The authors suggest that exhumation of CBU packages occurred
402 shortly after juxtaposition near peak metamorphic conditions.

403 Both Trotet et al. (2001a, 2001b) and Laurent et al. (2018) constrain high-P conditions for the CBU (> 2.0 GPa),
404 however, their proposed exhumation histories differ. Trotet et al. (2001b) suggested that CBU eclogites, blueschists and
405 greenschists underwent different T-t histories during exhumation and were juxtaposed late along ductile shear zones. Laurent
406 et al. (2018) suggested that the entire CBU reached peak metamorphic conditions of ~2.2 GPa, and that units that preserved
407 blueschist facies assemblages underwent cooling during decompression, whereas rocks of southern Syros from lower structural
408 levels experienced isobaric heating (~550 °C) at mid-crustal depths (~1.0 GPa) followed by subsequent cooling. Laurent et al.
409 (2018) interpreted reheating to indicate that CBU rocks on Syros reached high-P conditions, and then transitioned from a
410 forearc to back-arc setting at ~1.0 GPa, thus experiencing a period of increasing temperatures.

411 Skelton et al. (2018) also estimated peak and exhumation P-T conditions of rocks from Fabrikas (southern Syros),
412 and interpreted exhumation of the CBU within an extrusion wedge (Ring et al., 2020). The authors constrained maximum P-
413 T conditions of ~1.9 GPa and 540 °C, and retrograde conditions of ~1.4 – 1.6 GPa and 510 - 520 °C (blueschist facies) and
414 ~0.3 GPa and 450 °C (greenschist facies) based on Thermocalc end-member activity modeling (Powell and Holland, 1994).
415 Retrograde blueschist conditions (inferred from garnet growth) are similar between their estimates and ours, but greenschist
416 facies conditions vastly differ. However, Skelton et al. (2018) focused on greenschist facies outcrops wherein metamorphism
417 occurred locally over short length scales (e.g. ~10 - 100 m), adjacent to late-stage brittle normal faults. We interpret our D₂
418 stage of greenschist facies metamorphism to pre-date late-stage normal faulting that has been attributed to Neogene block
419 rotations (Cooperdock and Stockli, 2016) or possible coeval granitoid magmatism during Miocene back-arc extension (Keiter
420 et al., 2011).

421 Gyomlai et al. (2021) estimate max and retrograde P-T conditions, but from metasomatic rocks from the Kampos
422 belt in northern Syros. The authors estimated maximum T conditions of 561 ± 78 °C, and two retrograde pressure-temperature
423 conditions: 1.02 ± 0.15 GPa and 505 ± 155 °C, and 1.03 ± 0.11 GPa and 653 ± 27 °C. The retrograde pressures are reasonable
424 (~1.0 ± 0.1 - 0.2 GPa), but the max temperatures raise questions that the authors discuss. Specifically, temperatures above
425 ~600 °C (at ~1.0 GPa) would lead to serpentine breakdown (Guillot et al., 2015; Wunder and Schreyer, 1997); however,
426 serpentine is abundant across Syros. The authors used the 505 ± 155 °C temperature constraint, and a temperature below 600
427 °C, to suggest their studied rocks reached temperatures between 500 – 600 °C at ~1.0 GPa. Several other studies on retrograde
428 metasomatic rocks from Kampos constrain P-T conditions: ~1.17 – 1.23 GPa and 500 – 550 °C (Breeding et al., 2004), ~0.60
429 – 0.75 GPa and 400 – 430 °C (Marschall et al., 2006), and ~1.20 GPa and 430 °C (Miller et al., 2009). Breeding et al. (2004)
430 did not constrain a temperature, but used an estimated temperature from Trotet et al. (2001a), and constrained a pressure of
431 ~1.17 – 1.23 GPa at the estimated T of ~500 – 550 °C using Thermocalc V. 3.2. Marschall et al. (2006) used the garnet-
432 clinopyroxene thermometer and Thermocalc V. 3.01 to calculate temperatures, and estimated a pressure based on jadeite +
433 SiO₂ → albite reaction. Miller et al. (2009) used *Perple_X* and the thermodynamic database of Holland and Powell (1998) to
434 calculate P-T conditions from reaction zones. In general, most studies indicate cooling during decompression for metasomatic
435 rocks from Kampos, with the exception of interpretations by Gyomlai et al. (2021); however, the large uncertainty of their

436 temperature estimate (505 ± 155 °C) makes it difficult to differentiate between cooling during decompression, isothermal
437 decompression, or re-heating.

438 Our results show that rocks from Kalamisia, Delfini, Lotos, and Megas Gialos, reached peak P-T conditions and
439 underwent cooling during retrograde blueschist and greenschist facies metamorphism (Fig. 7a). Peak P-T conditions of the
440 CBU are $\sim 1.6 - 1.8$ GPa and $500 - 550$ °C (Group 1 qtz-in-grt P_{trap} estimates), indicating a subduction zone geothermal gradient
441 of $\sim 9 - 10$ °C km^{-1} at $\sim 55 - 60$ km (assuming 30 MPa km^{-1}). Group 2 and 3 qtz-in-ep P_{trap} estimates indicate geothermal gradients
442 of ~ 10 °C km^{-1} and ~ 12 °C km^{-1} at ~ 47 and 33 km depths, respectively (Fig. 7a), demonstrating a similar P-T trajectory during
443 exhumation. We do not have a temperature constraint for the ep1 population; however, we consider cooling during
444 decompression from garnet growth ($\sim 500 - 550$ °C) to ep2 growth (~ 400 °C), to be the most likely P-T path for CBU rocks
445 from Syros. Isothermal decompression from ~ 1.8 GPa and $\sim 500 - 550$ °C to ~ 1.0 GPa, would lead to terminal lawsonite
446 breakdown above ~ 450 °C and produce kyanite + zoisite (Hamelin et al., 2018; Schumacher et al., 2008); however, kyanite
447 has not been found on Syros, therefore requiring temperatures below ~ 450 °C at ~ 1.0 GPa. It is possible that sluggish kinetics
448 did not lead to lawsonite breakdown, but given the prevalent evidence of retrograde deformation on Syros and the extensive
449 presence of retrograde overprinting/mineral growth, we consider kinetic-limitations to be unlikely. Furthermore, the chemical
450 evolution of amphiboles (magnesio-riebeckite \rightarrow winchite \rightarrow actinolite) suggests that CBU rocks from Syros followed a cold
451 P-T path during decompression (c.f., Kotowski et al., 2020). Our P-T constraints are also inconsistent with reheating to ~ 550
452 °C and 1.0 GPa, wherein amphibolite facies mineralogy may be stable. Our samples and the sample from which Laurent et al.
453 (2018) determined reheating (SY1407), preserve no mineralogical evidence for having reached epidote-amphibolite facies
454 (Fig. 7b; e.g., pargasite/hornblende, biotite/muscovite). Instead, the matrix mineralogy of sample SY1407 (glaucophane,
455 phengite, rutile) suggests that these rocks formed under a cold geothermal gradient, rather than in a back-arc setting with an
456 elevated geothermal gradient. Laurent et al. (2018) suggest that sample SY1407 records albite-epidote-blueschist conditions,
457 a field metamorphic facies that can expand to higher T conditions; however, a pseudosection created for a similar bulk
458 composition suggests that the determined P-T constraints (~ 1.0 GPa and 550 °C) are within epidote-amphibolite facies (Trotet
459 et al., 2001a). Furthermore, results from sample SY1407 of Laurent et al. (2018) sometimes disagree when using local vs. bulk
460 compositions for modeling. Models that use bulk compositions and consider Mn suggest that the core and mantle of the garnet
461 record P-T conditions of ~ 1.8 GPa and 475 °C, whereas models that use local compositions or do not consider Mn suggest that
462 the garnets do not record conditions above ~ 1.0 GPa (model residuals are lower using local bulk composition models).

463 Our results suggest that rocks from different Syros outcrops record similar peak and exhumation P-T conditions, but
464 experienced different extents of deformation and thus recrystallization during exhumation. The similar peak pressures (> 0.8
465 GPa) between different Syros outcrops suggests that these rocks belong to the Upper Cycladic Blueschist Nappe (Grasemann
466 et al., 2018), even though in some cases significant retrogression overprinted indicators that would suggest these rocks reached
467 P conditions above ~ 0.8 GPa. The observation of similar P-T conditions reached at different locations is inconsistent with
468 results that suggest individual P-T paths for rocks that preserve different metamorphic facies (Trotet et al., 2001b, a), and
469 different sections of the CBU (Laurent et al., 2018); however, we do not have T constraints for rocks from southern Syros. Our

470 results are in better agreement with a P-T evolution resembling that of Schumacher et al. (2008), and a geothermal gradient of
471 $\sim 10 - 12 \text{ }^\circ\text{C km}^{-1}$ that has also been proposed for CBU rocks from Sifnos, Greece (Schmädicke and Will, 2003).

472 **6.4 Limitations of elastic thermobarometry**

473 Elastic thermobarometry has rapidly gained interest due to its limited dependence on mineral and fluid chemistry.
474 Recent hydrostatic experiments that grow garnet around quartz have also shown the quartz-in-garnet barometer is accurate
475 from $\sim 0.8 - 3.0 \text{ GPa}$ ($\pm 0.1 - 0.2 \text{ GPa}$, Thomas and Spear, 2018; Bonazzi et al., 2019). The results suggest that the applied 1-
476 dimensional elastic model that assumes a spherical inclusion and isotropic inclusion-host pairs (Guiraud and Powell, 2006;
477 Angel et al., 2017b), and the currently applied EoS' (Angel et al., 2017a; Holland and Powell, 2011; Milani et al., 2017),
478 sufficiently replicate the elastic behaviour of an isotropic mineral (quartz) in a near isotropic host (garnet). Nonetheless,
479 multiple secondary processes may affect quartz-in-garnet entrapment conditions: 1) mineral anisotropy (e.g., Murri et al.,
480 2018), 2) inclusion shape effects (e.g., Cesare et al., 2021; Mazzucchelli et al., 2018), 3) relaxation adjacent to fractures or the
481 host exterior, or overpressures adjacent to other inclusions (e.g., Zhong et al., 2020), 4) non-ideal tensile strain (e.g., Cisneros
482 and Befus, 2020), or 5) non-elastic strain (i.e., viscous strain, e.g., Zhang, 1998). We propose that none of these processes have
483 affected our quartz-in-garnet barometry results for the following reasons: 1) P_{inc} values calculated from different quartz bands
484 and by accounting for anisotropy (strains) center around the hydrostatic stress lines (1:1 line, Fig. 5), and P_{inc} calculated from
485 strains changes the final P_{trap} by $< 0.2 \text{ GPa}$ (relative to P_{inc} calculated from the 464 cm^{-1} band). 2) Near spherical quartz
486 inclusions were analysed to minimize shape effects, and measurements were taken from the center of quartz inclusions to avoid
487 stress effects at inclusion-host boundaries. 3) Quartz inclusions were a minimum two-to-three-times the radial distance away
488 from fractures, cleavage, and the host exterior, or other inclusions to minimize under- or overpressures, respectively. 4) All
489 quartz inclusions from this study exist under compression, thus tensile strain limits are not relevant. 5) The maximum estimated
490 temperature of CBU rocks from Syros is $\sim 500 - 550 \text{ }^\circ\text{C}$, and garnet flow laws predict that viscous creep of garnet occurs above
491 $\sim 650 \text{ }^\circ\text{C}$ at geologic strain rates (Wang and Ji, 2001; Ji and Martignole, 1994); therefore, viscous strain of garnet is unlikely
492 to have occurred. Considering the current state-of-knowledge in elastic thermobarometry, we propose that our pressure results
493 have been minimally influenced by secondary effects.

494 In contrast, the quartz-in-epidote barometer is less studied. Recent studies have explored the suitability of using an
495 isotropic elastic model to model the elastic evolution of two anisotropic minerals (Cisneros et al., 2020). Results showed that
496 an isotropic elastic model suitably simulates the pressure evolution of two anisotropic minerals during heating, and that the
497 calculated entrapment pressures agree with independent thermobarometry constraints. However, it is unknown if isotropic
498 elastic models correctly simulate the elastic evolution of anisocoric mineral pairs during compression, and additional processes
499 may influence the entrapment pressures calculated from quartz-inclusions-in-epidote: 1) the orientation of quartz inclusions
500 relative to the orientation of epidote, and 2) the material properties of epidote (i.e., at what conditions does viscous creep
501 become important for epidote). 1) Cisneros et al. (2020) showed that the orientation of quartz inclusions relative to epidote
502 may have had a minimal effect on the elastic evolution of quartz-epidote pairs, but the orientation of quartz and epidote were

503 not determined. We hypothesize that in this study, the mutual orientation of quartz-epidote inclusion-host pairs had a minimal
504 effect on the calculated entrapment pressures. If the mutual orientation of quartz-epidote pairs had a large effect, we expect
505 that the P_{inc} calculated from different quartz-inclusions-in-epidote would exhibit significant scatter; however, P_{inc} values from
506 different quartz-inclusions-in-epidote are similar, and P_{inc} values from different quartz bands and strains, center around the
507 hydrostatic stress line (Fig. 5). The P_{inc} scatter from different quartz-inclusions-in-epidote (same ep population, e.g., ep2) and
508 the P_{inc} variation from different quartz bands and strains, generally does not exceed that of quartz-inclusions-in-garnet. The
509 minimal P_{inc} variation between quartz-inclusions-in-epidote from the same epidote population may result from the orientation
510 of quartz and epidote parallel to the primary foliation. The orientation of quartz-epidote pairs may lead to a bulk stress tensor
511 that produces minimal orientation-dependent effects, or the lower bulk modulus of epidote (relative to garnet) may result in a
512 small stress anisotropy. 2) No epidote flow law exists (to the best of our knowledge); therefore, the temperature at which
513 viscous strain will be important for epidote is unknown. Nonetheless, in contrast to garnet (isotropic), evidence for viscous
514 creep in epidote can be observed in thin section. In epidotes from this study, we have observed no thin-section scale evidence
515 of dislocation creep; however, μm -scale viscous creep in epidote adjacent to quartz inclusions cannot be excluded.

516 **6.5 Implications for exhumation mechanisms**

517 Our results indicate that the CBU followed a “cooling during decompression” P-T trajectory that required a heat sink
518 at depth to cool rocks during exhumation. Cooling could be achieved under a steady-state subduction zone thermal gradient
519 with slab-top temperatures similar to those of warm subduction zones, such as in Cascadia (e.g., Syracuse et al., 2010;
520 Walowski et al., 2015). This would suggest that exhumation was achieved parallel to the subducting plate, in a subduction
521 channel geometry prior to core-complex formation. Results from this study cannot differentiate between extrusion wedge
522 models (“extrusion” of a wedge of CBU rocks within a subduction channel) that require a kinematically necessary thrust fault
523 at the base (the subducting slab) and a kinematically necessary normal fault at the top (upper plate), and other general
524 subduction channel models (e.g., Ring et al., 2020). Subduction channel and extrusion models have slight differences, i.e., the
525 extrusion wedge model calls for a specific geometry that should produce opposing shear sense indicators at distinct locations
526 that define the base (subduction plate) and top (upper plate) of the wedge (within a subduction channel). A subduction channel
527 model has a looser definition (without a specific geometric structure) that merely reflects the plate interface structure (discrete
528 or broad interface), and does not require this deformation. Because we do not present sufficient kinematic information in this
529 study to differentiate these models, we prefer to use a general “subduction channel” model nomenclature, to indicate that we
530 interpret CBU rocks to have been exhumed parallel to the subducting plate, within a broad, viscous shear zone that defines the
531 subduction interface.

532 During this phase of exhumation, CBU rocks remained within a cold forearc until they reached the mid-crust (~1.0
533 GPa), and exhibit a progressive change in kinematics, from N-S stretching lineations during subduction (e.g., Behr et al., 2018;
534 Laurent et al., 2016; Philippon et al., 2011), to lineations that swing towards the NE (this study, Roche et al., 2016: Sifnos)
535 and E-W during exhumation (c.f., Kotowski and Behr, 2019; Laurent et al., 2016). We propose that N-S (D_s) lineations

536 (subduction-related) and exhumation-related upright folds that generate NE (D_{11}) and E-W (D_{12}) extension parallel to fold hinge
537 lines, document the transition from subduction to exhumation as rocks turn the corner to be exhumed within the subduction
538 channel. Stretching lineations in the footwall of the North and West Cycladic Detachment Systems have top-to-the- NE and
539 SW orientations, respectively (e.g., Bricchau et al., 2007; Grasemann et al., 2012; Jolivet et al., 2010; Mehl et al., 2005). The
540 inferred P-T conditions and kinematics of our studied samples are consistent with Syros recording early deformation and
541 metamorphism within a forearc setting, whereas adjacent Cycladic islands that border the North and West Cycladic
542 Detachment Systems record late-stage kinematics and greenschist facies metamorphism that capture the CBU transition to a
543 warmer back-arc setting (e.g., Laurent et al., 2016; Ring et al., 2020; Roche et al., 2016; Schmädicke and Will, 2003). Our
544 data suggests that during generation of exhumation-related upright folds (D_{11-12}), rocks from the CBU on southern Syros (below
545 the Kampos nappe) followed similar P-T conditions exhumation (Fig. 7). It is unclear if the upper Kampos nappe exhibited
546 the same deformation because it preserves less structural coherency; however, rocks from Kampos and southern Syros seem
547 to have experienced similar P-T conditions during exhumation. Rocks from different sections of the CBU may have reached
548 peak P conditions at different times, and thus experienced the same exhumation-related deformation at different times
549 (Kotowski et al., 2020); however, our data suggest that rocks from different sections of the southern CBU on Syros were
550 exhumed within a forearc setting up to ~33 km depth. We propose that CBU on Syros may not record back-arc deformation
551 until the Vari detachment accommodated exhumation of the CBU at ~10 – 8 Ma (~5 - 7 km depth, Soukis and Stockli, 2013).
552 Back-arc related deformation occurs directly adjacent to the Vari detachment, as evidenced by semi-brittle to brittle cataclastic
553 deformation (greenschist facies) that affects the Upper Unit and the underlying CBU (Soukis and Stockli, 2013).

554 7. Conclusions

555 This work highlights the potential of using elastic thermobarometry in combination with structural (macro and micro)
556 and petrographic constraints, to better constrain P-T conditions of challenging rock assemblages. Our results allow us to place
557 robust P-T constraints on distinct textural fabrics that are related to well-constrained outcrop scale structures. In particular, the
558 work highlights how the qtz-in-ep barometer is well suited for constraining formation conditions of epidote, a common mineral
559 that is found within a large range of geologic settings and P-T conditions. Combining the qtz-in-ep barometer with other elastic
560 thermobarometers (e.g., qtz-in-grt) allows determination of protracted P-T histories from minerals that record different
561 geologic stages within single rocks samples.

562 Our new results show that CBU rocks from Syros, Greece, experienced similar P-T conditions during subduction and
563 exhumation, inconsistent with results that suggest different P-T histories for CBU rocks for Syros or increasing temperatures
564 during exhumation. Our targeted stages of deformation and metamorphism suggest that CBU rocks from Syros record cooling
565 during decompression, consistent with exhumation within a subduction channel and early deformation and metamorphism
566 within a forearc (at least to ~33 km depth), prior to Miocene core-complex formation and transition to a warmer back-arc
567 setting.

568 Appendix A: Stable isotope temperature error calculations

569 Temperature errors from oxygen isotope measurements were calculated through the square-root of the summed
570 quadratures of all sources of uncertainty. These uncertainties included error of $\delta^{18}\text{O}$ values of quartz (qtz) and calcite (cc) of \pm
571 0.1 ‰ (1 σ) and \pm 0.04 ‰ (1 σ), respectively, and errors associated with the Sharp and Kirschner (1994) quartz-calcite oxygen
572 isotope fractionation calibration (A parameter). Errors from the sum of propagated analytical errors, were propagated through
573 the empirical calibration of quartz-calcite oxygen isotope fraction that was used for temperature calculations:

$$574 \Delta_{qtz-cc} = \frac{A \times 10^6}{T^2} \quad \#A1$$

575
576 where $A = 0.87 \pm 0.06$ (1 σ). The square-root of the summed quadratures is expressed as:

$$577 \sigma_T = \sqrt{\sigma_A^2 \left(\frac{\partial T}{\partial A}\right)^2 + \sigma_{\Delta_{qtz-cc}}^2 \left(\frac{\partial T}{\partial \Delta_{qtz-cc}}\right)^2} \quad \#A2$$

$$578
579 \sigma_T = \sqrt{\sigma_A^2 \left(\frac{0.5 * 10^3}{\sqrt{A} * \sqrt{\Delta_{qtz-cc}}}\right)^2 + \sigma_{\Delta_{qtz-cc}}^2 \left(-0.5 * \frac{\sqrt{A} * 10^3}{\Delta_{qtz-cc}^{1.5}}\right)^2} \quad \#A3$$

580 Author Contribution

581 All authors contributed to this manuscript. M. Cisneros developed the epidote barometer, collected the data, and wrote
582 the manuscript. J. Barnes, W. Behr, A. Kotowski, D. Stockli, and K. Soukis helped with conceiving the project, field work,
583 and writing.

584 Acknowledgements

585 We thank J. Schumacher and V. Laurent for constructive reviews that helped improve this manuscript, and F. Rossetti
586 for editorial handling **and additional comments that helped improve this manuscript**. We thank N. Raia for field work
587 assistance, J. Allaz for assistance on the microprobe at ETH Zürich, and C. Farley and R. Bobnar for access to the Raman
588 Spectrometer at Virginia Tech. This work was supported by a GSA Student Research Grant and a Ford Foundation Fellowship
589 awarded to M.C, an NSF Graduate Research Fellowship awarded to A.K., and NSF Grant (EAR-1725110) awarded to J.B.,
590 W.B., and D.S.

591 **References**

- 592 Adams, H. G., Cohen, L. H., and Rosenfeld, J. L.: Solid inclusion piezothermometry I: comparison dilatometry, 60, 574–583,
593 1975a.
- 594 Adams, H. G., Cohen, L. H., and Rosenfeld, J. L.: Solid inclusion piezothermometry II: geometric basis, calibration for the
595 association quartz-garnet, and application to some pelitic schists, 60, 584–598, 1975b.
- 596 Alvaro, M., Mazzucchelli, M. L., Angel, R. J., Murri, M., Campomenosi, N., Scambelluri, M., Nestola, F., Korsakov, A.,
597 Tomilenko, A. A., Marone, F., and Morana, M.: Fossil subduction recorded by quartz from the coesite stability field, *Geology*,
598 48, 24–28, <https://doi.org/10.1130/G46617.1>, 2020.
- 599 Angel, R. J., Alvaro, M., Miletich, R., and Nestola, F.: A simple and generalised P-T-V EoS for continuous phase transitions,
600 implemented in EosFit and applied to quartz, *Contrib Mineral Petrol*, 172, 29, <https://doi.org/10.1007/s00410-017-1349-x>,
601 2017a.
- 602 Angel, R. J., Mazzucchelli, M. L., Alvaro, M., and Nestola, F.: EosFit-Pinc: A simple GUI for host-inclusion elastic
603 thermobarometry, 102, 1957–1960, <http://dx.doi.org/10.2138/am-2017-6190>, 2017b.
- 604 Angel, R. J., Murri, M., Mihailova, B., and Alvaro, M.: Stress, strain and Raman shifts, 234, 129–140,
605 <https://doi.org/10.1515/zkri-2018-2112>, 2019.
- 606 Ashley, K. T., Caddick, M. J., Steele-MacInnis, M. J., Bodnar, R. J., and Dragovic, B.: Geothermobarometric history of
607 subduction recorded by quartz inclusions in garnet, *Geochemistry, Geophysics, Geosystems*, 15, 350–360,
608 <https://doi.org/10.1002/2013GC005106>, 2014.
- 609 Ashley, K. T., Steele-MacInnis, M., Bodnar, R. J., and Darling, R. S.: Quartz-in-garnet inclusion barometry under fire:
610 Reducing uncertainty from model estimates, *Geology*, 44, 699–702, <https://doi.org/10.1130/G38211.1>, 2016.
- 611 Augier, R., Jolivet, L., Gadenne, L., Lahfid, A., and Driussi, O.: Exhumation kinematics of the Cycladic Blueschists unit and
612 back-arc extension, insight from the Southern Cyclades (Sikinos and Folegandros Islands, Greece), 34, 152–185,
613 <https://doi.org/10.1002/2014TC003664>, 2015.
- 614 Avigad, D.: High-pressure metamorphism and cooling on SE Naxos (Cyclades, Greece), *European Journal of Mineralogy*, 10,
615 1309–1319, 1998.
- 616 Baxter, E. F.: Natural constraints on metamorphic reaction rates, 220, 183–202,
617 <https://doi.org/10.1144/GSL.SP.2003.220.01.11>, 2003.
- 618 Behr, W. M., Kotowski, A. J., and Ashley, K. T.: Dehydration-induced rheological heterogeneity and the deep tremor source
619 in warm subduction zones, *Geology*, 46, 475–478, <https://doi.org/10.1130/G40105.1>, 2018.
- 620 Berman, R. G.: Thermobarometry using multi-equilibrium calculations; a new technique, with petrological applications, *The*
621 *Canadian Mineralogist*, 29, 833–855, 1991.
- 622 Bonazzi, M., Tumiati, S., Thomas, J., Angel, R. J., and Alvaro, M.: Assessment of the reliability of elastic geobarometry with
623 quartz inclusions, *Lithos*, 105201, <https://doi.org/10.1016/j.lithos.2019.105201>, 2019.

624 Breeding, C. M., Ague, J. J., and Bröcker, M.: Fluid–metasedimentary rock interactions in subduction-zone mélange:
625 Implications for the chemical composition of arc magmas, *Geology*, 32, 1041–1044, <https://doi.org/10.1130/G20877.1>, 2004.

626 Brichau, S., Ring, U., Carter, A., Monié, P., Bolhar, R., Stockli, D., and Brunel, M.: Extensional faulting on Tinos Island,
627 Aegean Sea, Greece: How many detachments?, 26, <https://doi.org/10.1029/2006TC001969>, 2007.

628 Bröcker, M. and Franz, L.: Dating metamorphism and tectonic juxtaposition on Andros Island (Cyclades, Greece): results of
629 a Rb–Sr study, 143, 609–620, <https://doi.org/10.1017/S001675680600241X>, 2006.

630 Bröcker, M., Kreuzer, H., Matthews, A., and Okrusch, M.: 40Ar/39Ar and oxygen isotope studies of polymetamorphism from
631 Tinos Island, Cycladic blueschist belt, Greece, 11, 223–240, <https://doi.org/10.1111/j.1525-1314.1993.tb00144.x>, 1993.

632 Bröcker, M., Baldwin, S., and Arkudas, R.: The geological significance of 40Ar/39Ar and Rb–Sr white mica ages from Syros
633 and Sifnos, Greece: a record of continuous (re)crystallization during exhumation?, 31, 629–646,
634 <https://doi.org/10.1111/jmg.12037>, 2013.

635 Campomenosi, N., Mazzucchelli, M. L., Mihailova, B., Scambelluri, M., Angel, R. J., Nestola, F., Reali, A., and Alvaro, M.:
636 How geometry and anisotropy affect residual strain in host-inclusion systems: Coupling experimental and numerical
637 approaches, 103, 2032–2035, <https://doi.org/10.2138/am-2018-6700CCBY>, 2018.

638 Carlson, W. D.: Scales of disequilibrium and rates of equilibration during metamorphism, *American Mineralogist*, 87, 185–
639 204, <https://doi.org/10.2138/am-2002-2-301>, 2002.

640 Cesare, B., Parisatto, M., Mancini, L., Peruzzo, L., Franceschi, M., Tacchetto, T., Reddy, S., Spiess, R., Nestola, F., and
641 Marone, F.: Mineral inclusions are not immutable: Evidence of post-entrapment thermally-induced shape change of quartz in
642 garnet, *Earth and Planetary Science Letters*, 555, 116708, <https://doi.org/10.1016/j.epsl.2020.116708>, 2021.

643 Cisneros, M. and Befus, K. S.: Applications and Limitations of Elastic Thermobarometry: Insights From Elastic Modeling of
644 Inclusion-Host Pairs and Example Case Studies, 21, e2020GC009231, <https://doi.org/10.1029/2020GC009231>, 2020.

645 Cisneros, M., Ashley, K. T., and Bodnar, R. J.: Evaluation and application of the quartz-inclusions-in-epidote mineral
646 barometer, *American Mineralogist*, 105, 1140–1151, <https://doi.org/10.2138/am-2020-7379>, 2020.

647 Cliff, R. A., Bond, C. E., Butler, R. W. H., and Dixon, J. E.: Geochronological challenges posed by continuously developing
648 tectonometamorphic systems: insights from Rb–Sr mica ages from the Cycladic Blueschist Belt, Syros (Greece), 35, 197–211,
649 <https://doi.org/10.1111/jmg.12228>, 2017.

650 Cooperdock, E. H. G. and Stockli, D. F.: Unraveling alteration histories in serpentinites and associated ultramafic rocks with
651 magnetite (U-Th)/He geochronology, *Geology*, 44, 967–970, <https://doi.org/10.1130/G38587.1>, 2016.

652 Dragovic, B., Samanta, L. M., Baxter, E. F., and Selverstone, J.: Using garnet to constrain the duration and rate of water-
653 releasing metamorphic reactions during subduction: An example from Sifnos, Greece, 314–317, 9–22,
654 <https://doi.org/10.1016/j.chemgeo.2012.04.016>, 2012.

655 Dragovic, B., Baxter, E. F., and Caddick, M. J.: Pulsed dehydration and garnet growth during subduction revealed by zoned
656 garnet geochronology and thermodynamic modeling, Sifnos, Greece, *Earth and Planetary Science Letters*, 413, 111–122,
657 <https://doi.org/10.1016/j.epsl.2014.12.024>, 2015.

658 Enami, M., Nishiyama, T., and Mouri, T.: Laser Raman microspectrometry of metamorphic quartz: A simple method for
659 comparison of metamorphic pressures, *American Mineralogist*, 92, 1303–1315, <https://doi.org/10.2138/am.2007.2438>, 2007.

660 Essene, E. J.: The current status of thermobarometry in metamorphic rocks, 43, 1–44,
661 <https://doi.org/10.1144/GSL.SP.1989.043.01.02>, 1989.

662 Franz, G. and Liebscher, A.: Physical and Chemical Properties of the Epidote Minerals—An Introduction—, *Reviews in*
663 *Mineralogy and Geochemistry*, 56, 1–81, <https://doi.org/10.2138/gsrmg.56.1.1>, 2004.

664 Gatta, G. D., Merlini, M., Lee, Y., and Poli, S.: Behavior of epidote at high pressure and high temperature: a powder diffraction
665 study up to 10 GPa and 1,200 K, *Phys Chem Minerals*, 38, 419–428, <https://doi.org/10.1007/s00269-010-0415-y>, 2011.

666 Gautier, P., Brun, J.-P., and Jolivet, L.: Structure and kinematics of Upper Cenozoic extensional detachment on Naxos and
667 Paros (Cyclades Islands, Greece), 12, 1180–1194, <https://doi.org/10.1029/93TC01131>, 1993.

668 Grasemann, B., Schneider, D. A., Stöckli, D. F., and Iglseider, C.: Miocene bivergent crustal extension in the Aegean: Evidence
669 from the western Cyclades (Greece), *Lithosphere*, 4, 23–39, <https://doi.org/10.1130/L164.1>, 2012.

670 Grasemann, B., Huet, B., Schneider, D. A., Rice, A. H. N., Lemonnier, N., and Tschegg, C.: Miocene postorogenic extension
671 of the Eocene synorogenic imbricated Hellenic subduction channel: New constraints from Milos (Cyclades, Greece), *GSA*
672 *Bulletin*, 130, 238–262, <https://doi.org/10.1130/B31731.1>, 2018.

673 Groppo, C., Forster, M., Lister, G., and Compagnoni, R.: Glaucofane schists and associated rocks from Sifnos (Cyclades,
674 Greece): New constraints on the P–T evolution from oxidized systems, *Lithos*, 109, 254–273,
675 <https://doi.org/10.1016/j.lithos.2008.10.005>, 2009.

676 Guillot, S., Schwartz, S., Reynard, B., Agard, P., and Prigent, C.: Tectonic significance of serpentinites, *Tectonophysics*, 646,
677 1–19, <https://doi.org/10.1016/j.tecto.2015.01.020>, 2015.

678 Guiraud, M. and Powell, R.: P–V–T relationships and mineral equilibria in inclusions in minerals, *Earth and Planetary Science*
679 *Letters*, 244, 683–694, <https://doi.org/10.1016/j.epsl.2006.02.021>, 2006.

680 Gupta, S. and Bickle, M. J.: Ductile shearing, hydrous fluid channelling and high-pressure metamorphism along the basement-
681 cover contact on Sikinos, Cyclades, Greece, 224, 161–175, <https://doi.org/10.1144/GSL.SP.2004.224.01.11>, 2004.

682 Gyomlai, T., Agard, P., Marschall, H. R., Jolivet, L., and Gerdes, A.: Metasomatism and deformation of block-in-matrix
683 structures in Syros: The role of inheritance and fluid-rock interactions along the subduction interface, *Lithos*, 386–387, 105996,
684 <https://doi.org/10.1016/j.lithos.2021.105996>, 2021.

685 Hamelin, C., Brady, J. B., Cheney, J. T., Schumacher, J. C., Able, L. M., and Sperry, A. J.: Pseudomorphs after lawsonite from
686 Syros, Greece, <https://doi.org/10.1093/petrology/egy099>, 2018.

687 Holland, T. and Powell, R.: An internally consistent thermodynamic data set for phases of petrological interest, 16, 309–343,
688 <https://doi.org/10.1111/j.1525-1314.1998.00140.x>, 1998.

689 Holland, T. and Powell, R.: An improved and extended internally consistent thermodynamic dataset for phases of petrological
690 interest, involving a new equation of state for solids, 29, 333–383, <https://doi.org/10.1111/j.1525-1314.2010.00923.x>, 2011.

691 Isaak, D. G., Anderson, O. L., and Oda, H.: High-temperature thermal expansion and elasticity of calcium-rich garnets, *Phys*
692 *Chem Minerals*, 19, 106–120, <https://doi.org/10.1007/BF00198608>, 1992.

693 Jamtveit, B., Austrheim, H., and Putnis, A.: Disequilibrium metamorphism of stressed lithosphere, *Earth-Science Reviews*,
694 154, 1–13, <https://doi.org/10.1016/j.earscirev.2015.12.002>, 2016.

695 Javoy, M.: Stable isotopes and geothermometry, 133, 609–636, <https://doi.org/10.1144/gsjgs.133.6.0609>, 1977.

696 Ji, S. and Martignole, J.: Ductility of garnet as an indicator of extremely high temperature deformation, *Journal of Structural*
697 *Geology*, 16, 985–996, [https://doi.org/10.1016/0191-8141\(94\)90080-9](https://doi.org/10.1016/0191-8141(94)90080-9), 1994.

698 Jolivet, L. and Brun, J.-P.: Cenozoic geodynamic evolution of the Aegean, *Int J Earth Sci (Geol Rundsch)*, 99, 109–138,
699 <https://doi.org/10.1007/s00531-008-0366-4>, 2010.

700 Jolivet, L., Lecomte, E., Huet, B., Denèle, Y., Lacombe, O., Labrousse, L., Le Pourhiet, L., and Mehl, C.: The North Cycladic
701 Detachment System, *Earth and Planetary Science Letters*, 289, 87–104, <https://doi.org/10.1016/j.epsl.2009.10.032>, 2010.

702 Keiter, M., Ballhaus, C., and Tomaschek, F.: A new geological map of the Island of Syros (Aegean Sea, Greece): implications
703 for lithostratigraphy and structural history of the Cycladic Blueschist Unit, *Geological Society of America*, 2011.

704 Kohn, M. J. and Spear, F.: Retrograde net transfer reaction insurance for pressure-temperature estimates, *Geology*, 28, 1127–
705 1130, [https://doi.org/10.1130/0091-7613\(2000\)28<1127:RNTRIF>2.0.CO;2](https://doi.org/10.1130/0091-7613(2000)28<1127:RNTRIF>2.0.CO;2), 2000.

706 Kotowski, A. J. and Behr, W. M.: Length scales and types of heterogeneities along the deep subduction interface: Insights
707 from exhumed rocks on Syros Island, Greece, *Geosphere*, 15, 1038–1065, <https://doi.org/10.1130/GES02037.1>, 2019.

708 Kotowski, A. J., Behr, W. M., Cisneros, M., Stockli, D. F., Soukis, K., Barnes, J. D., and Ortega-Arroyo, D.: Subduction,
709 underplating, and return flow recorded in the Cycladic Blueschist Unit exposed on Syros Island, Greece,
710 <http://dx.doi.org/10.1002/essoar.10504307.1>, 2020.

711 Lagos, M., Scherer, E. E., Tomaschek, F., Münker, C., Keiter, M., Berndt, J., and Ballhaus, C.: High precision Lu–Hf
712 geochronology of Eocene eclogite-facies rocks from Syros, Cyclades, Greece, *Chemical Geology*, 243, 16–35,
713 <https://doi.org/10.1016/j.chemgeo.2007.04.008>, 2007.

714 Lamont, T. N., Searle, M. P., Gopon, P., Roberts, N. M. W., Wade, J., Palin, R. M., and Waters, D. J.: The Cycladic Blueschist
715 Unit on Tinos, Greece: Cold NE Subduction and SW Directed Extrusion of the Cycladic Continental Margin Under the
716 Tsiknias Ophiolite, 39, e2019TC005890, <https://doi.org/10.1029/2019TC005890>, 2020.

717 Lanari, P., Giuntoli, F., Loury, C., Burn, M., and Engi, M.: An inverse modeling approach to obtain P–T conditions of
718 metamorphic stages involving garnet growth and resorption, *European Journal of Mineralogy*, 29, 181–199,
719 <https://doi.org/10.1127/ejm/2017/0029-2597>, 2017.

720 Laurent, V., Jolivet, L., Roche, V., Augier, R., Scaillet, S., and Cardello, G. L.: Strain localization in a fossilized subduction
721 channel: Insights from the Cycladic Blueschist Unit (Syros, Greece), 672–673, 150–169,
722 <https://doi.org/10.1016/j.tecto.2016.01.036>, 2016.

723 Laurent, V., Huet, B., Labrousse, L., Jolivet, L., Monié, P., and Augier, R.: Extraneous argon in high-pressure metamorphic
724 rocks: Distribution, origin and transport in the Cycladic Blueschist Unit (Greece), *Lithos*, 272–273, 315–335,
725 <https://doi.org/10.1016/j.lithos.2016.12.013>, 2017.

726 Laurent, V., Lanari, P., Naïr, I., Augier, R., Lahfid, A., and Jolivet, L.: Exhumation of eclogite and blueschist (Cyclades,
727 Greece): Pressure–temperature evolution determined by thermobarometry and garnet equilibrium modelling, *Journal of*
728 *Metamorphic Geology*, 36, 769–798, <https://doi.org/10.1111/jmg.12309>, 2018.

729 Liati, A. and Seidel, E.: Metamorphic evolution and geochemistry of kyanite eclogites in central Rhodope, northern Greece,
730 *Contrib Mineral Petrol*, 123, 293–307, <https://doi.org/10.1007/s004100050157>, 1996.

731 Lister, G. S. and Forster, M. A.: White mica $40\text{Ar}/39\text{Ar}$ age spectra and the timing of multiple episodes of high-P metamorphic
732 mineral growth in the Cycladic eclogite–blueschist belt, Syros, Aegean Sea, Greece, *Journal of Metamorphic Geology*, 34,
733 401–421, <https://doi.org/10.1111/jmg.12178>, 2016.

734 Marschall, H. R.: Syros Metasomatic Tourmaline: Evidence for Very High- $\delta^{11}\text{B}$ Fluids in Subduction Zones, 47, 1915–1942,
735 <https://doi.org/10.1093/petrology/egl031>, 2006.

736 Marschall, H. R., Ludwig, T., Altherr, R., Kalt, A., and Tonarini, S.: Syros Metasomatic Tourmaline: Evidence for Very High-
737 $\delta^{11}\text{B}$ Fluids in Subduction Zones, *Journal of Petrology*, 47, 1915–1942, <https://doi.org/10.1093/petrology/egl031>, 2006.

738 Matthews, A. and Schliestedt, M.: Evolution of the blueschist and greenschist facies rocks of Sifnos, Cyclades, Greece, *Contr.*
739 *Mineral. and Petrol.*, 88, 150–163, <https://doi.org/10.1007/BF00371419>, 1984.

740 Mazzucchelli, M. L., Burnley, P., Angel, R. J., Morganti, S., Domeneghetti, M. C., Nestola, F., and Alvaro, M.: Elastic
741 geothermobarometry: Corrections for the geometry of the host-inclusion system, *Geology*, 46, 231–234,
742 <https://doi.org/10.1130/G39807.1>, 2018.

743 Mehl, C., Jolivet, L., and Lacombe, O.: From ductile to brittle: Evolution and localization of deformation below a crustal
744 detachment (Tinos, Cyclades, Greece), 24, <https://doi.org/10.1029/2004TC001767>, 2005.

745 Milani, S., Angel, R. J., Scandolo, L., Mazzucchelli, M. L., Ballaran, T. B., Klemme, S., Domeneghetti, M. C., Miletich, R.,
746 Scheidl, K. S., Derzsi, M., Tokár, K., Prencipe, M., Alvaro, M., and Nestola, F.: Thermo-elastic behavior of grossular garnet
747 at high pressures and temperatures, *American Mineralogist*, 102, 851–859, <https://doi.org/10.2138/am-2017-5855>, 2017.

748 Miller, D. P., Marschall, H. R., and Schumacher, J. C.: Metasomatic formation and petrology of blueschist-facies hybrid rocks
749 from Syros (Greece): Implications for reactions at the slab–mantle interface, *Lithos*, 107, 53–67,
750 <https://doi.org/10.1016/j.lithos.2008.07.015>, 2009.

751 Murri, M., Mazzucchelli, M. L., Campomenosi, N., Korsakov, A. V., Prencipe, M., Mihailova, B. D., Scambelluri, M., Angel,
752 R. J., and Alvaro, M.: Raman elastic geobarometry for anisotropic mineral inclusions, 103, 1869–1872,
753 <https://doi.org/10.2138/am-2018-6625CCBY>, 2018.

754 Murri, M., Alvaro, M., Angel, R. J., Prencipe, M., and Mihailova, B. D.: The effects of non-hydrostatic stress on the structure
755 and properties of alpha-quartz, *Phys Chem Minerals*, <https://doi.org/10.1007/s00269-018-01018-6>, 2019.

756 Nye, J. F.: Physical properties of crystals: their representation by tensors and matrices, Oxford university press, 1985.

757 Parra, T., Vidal, O., and Jolivet, L.: Relation between the intensity of deformation and retrogression in blueschist metapelites
758 of Tinos Island (Greece) evidenced by chlorite–mica local equilibria, *Lithos*, 63, 41–66, [https://doi.org/10.1016/S0024-](https://doi.org/10.1016/S0024-4937(02)00115-9)
759 [4937\(02\)00115-9](https://doi.org/10.1016/S0024-4937(02)00115-9), 2002.

760 Pattison, D. R. M., Chacko, T., Farquhar, J., and McFARLANE, C. R. M.: Temperatures of Granulite-facies Metamorphism:
761 Constraints from Experimental Phase Equilibria and Thermobarometry Corrected for Retrograde Exchange, *J Petrology*, 44,
762 867–900, <https://doi.org/10.1093/petrology/44.5.867>, 2003.

763 Pawley, A. R., Redfern, S. A. T., and Holland, T. J. B.: Volume behavior of hydrous minerals at high pressure and temperature:
764 I. Thermal expansion of lawsonite, zoisite, clinozoisite, and diaspore, 81, 335–340, <https://doi.org/10.2138/am-1996-3-407>,
765 1996.

766 Peacock, S. M.: The importance of blueschist → eclogite dehydration reactions in subducting oceanic crust, *GSA Bulletin*,
767 105, 684–694, [https://doi.org/10.1130/0016-7606\(1993\)105<0684:TIOBED>2.3.CO;2](https://doi.org/10.1130/0016-7606(1993)105<0684:TIOBED>2.3.CO;2), 1993.

768 Peillod, A., Ring, U., Glodny, J., and Skelton, A.: An Eocene/Oligocene blueschist-/greenschist facies P–T loop from the
769 Cycladic Blueschist Unit on Naxos Island, Greece: Deformation-related re-equilibration vs. thermal relaxation, 35, 805–830,
770 <https://doi.org/10.1111/jmg.12256>, 2017.

771 Peillod, A., Majka, J., Ring, U., Drüppel, K., Patten, C., Karlsson, A., Włodek, A., and Tehler, E.: Differences in
772 decompression of a high-pressure unit: A case study from the Cycladic Blueschist Unit on Naxos Island, Greece, *Lithos*, 386–
773 387, 106043, <https://doi.org/10.1016/j.lithos.2021.106043>, 2021.

774 Pe-Piper, G. and Piper, D. J. W.: The igneous rocks of Greece: The anatomy of an orogen, 2002.

775 Philippon, M., Brun, J.-P., and Gueydan, F.: Tectonics of the Syros blueschists (Cyclades, Greece): From subduction to Aegean
776 extension: TECTONICS OF THE SYROS BLUESCHISTS, 30, n/a-n/a, <https://doi.org/10.1029/2010TC002810>, 2011.

777 Powell, R. and Holland, T.: Optimal geothermometry and geobarometry, *American Mineralogist*, 79, 120–133, 1994.

778 Putlitz, B., Cosca, M. A., and Schumacher, J. C.: Prograde mica ⁴⁰Ar/³⁹Ar growth ages recorded in high pressure rocks
779 (Syros, Cyclades, Greece), *Chemical Geology*, 214, 79–98, <https://doi.org/10.1016/j.chemgeo.2004.08.056>, 2005.

780 Qin, F., Wu, X., Wang, Y., Fan, D., Qin, S., Yang, K., Townsend, J. P., and Jacobsen, S. D.: High-pressure behavior of natural
781 single-crystal epidote and clinozoisite up to 40 GPa, *Phys Chem Minerals*, 43, 649–659, [https://doi.org/10.1007/s00269-016-](https://doi.org/10.1007/s00269-016-0824-7)
782 [0824-7](https://doi.org/10.1007/s00269-016-0824-7), 2016.

783 Ridley, J.: Evidence of a temperature-dependent ‘blueschist’ to ‘eclogite’ transformation in high-pressure metamorphism of
784 metabasic rocks, 25, 852–870, 1984.

785 Ring, U., Glodny, J., Will, T., and Thomson, S.: The Hellenic Subduction System: High-Pressure Metamorphism, Exhumation,
786 Normal Faulting, and Large-Scale Extension, 38, 45–76, <https://doi.org/10.1146/annurev.earth.050708.170910>, 2010.

787 Ring, U., Pantazides, H., Glodny, J., and Skelton, A.: Forced Return Flow Deep in the Subduction Channel, Syros, Greece,
788 39, e2019TC005768, <https://doi.org/10.1029/2019TC005768>, 2020.

789 Roche, V., Laurent, V., Cardello, G. L., Jolivet, L., and Scaillet, S.: Anatomy of the Cycladic Blueschist Unit on Sifnos Island
790 (Cyclades, Greece), *Journal of Geodynamics*, 97, 62–87, <https://doi.org/10.1016/j.jog.2016.03.008>, 2016.

791 Rosenbaum, G., Avigad, D., and Sánchez-Gómez, M.: Coaxial flattening at deep levels of orogenic belts: evidence from
792 blueschists and eclogites on Syros and Sifnos (Cyclades, Greece), *Journal of Structural Geology*, 24, 1451–1462,
793 [https://doi.org/10.1016/S0191-8141\(01\)00143-2](https://doi.org/10.1016/S0191-8141(01)00143-2), 2002.

794 Rosenfeld, J. L.: Stress effects around quartz inclusions in almandine and the piezothermometry of coexisting aluminum
795 silicates, *Am J Sci*, 267, 317–351, <https://doi.org/10.2475/ajs.267.3.317>, 1969.

796 Rosenfeld, J. L. and Chase, A. B.: Pressure and temperature of crystallization from elastic effects around solid inclusions in
797 minerals?, *Am J Sci*, 259, 519–541, <https://doi.org/10.2475/ajs.259.7.519>, 1961.

798 Rubie, D. C.: Disequilibrium during metamorphism: the role of nucleation kinetics, 138, 199–214,
799 <https://doi.org/10.1144/GSL.SP.1996.138.01.12>, 1998.

800 Schliestedt, M. and Matthews, A.: Transformation of blueschist to greenschist facies rocks as a consequence of fluid
801 infiltration, Sifnos (Cyclades), Greece, *Contr. Mineral. and Petrol.*, 97, 237–250, <https://doi.org/10.1007/BF00371243>, 1987.

802 Schmädicke, E. and Will, T. M.: Pressure–temperature evolution of blueschist facies rocks from Sifnos, Greece, and
803 implications for the exhumation of high-pressure rocks in the Central Aegean, 21, 799–811, <https://doi.org/10.1046/j.1525->
804 1314.2003.00482.x, 2003.

805 Schmidt, C. and Ziemann, M. A.: In-situ Raman spectroscopy of quartz: A pressure sensor for hydrothermal diamond-anvil
806 cell experiments at elevated temperatures, *American Mineralogist*, 85, 1725–1734, <https://doi.org/10.2138/am-2000-11-1216>,
807 2000.

808 Schneider, D. A., Grasemann, B., Lion, A., Soukis, K., and Draganits, E.: Geodynamic significance of the Santorini
809 Detachment System (Cyclades, Greece), 30, 414–422, <https://doi.org/10.1111/ter.12357>, 2018.

810 Schumacher, J. C., Brady, J. B., Cheney, J. T., and Tonnsen, R. R.: Glaucofane-bearing Marbles on Syros, Greece, *J*
811 *Petrology*, 49, 1667–1686, <https://doi.org/10.1093/petrology/egn042>, 2008.

812 Sharp, Z. D.: A laser-based microanalytical method for the in situ determination of oxygen isotope ratios of silicates and
813 oxides, *Geochimica et Cosmochimica Acta*, 54, 1353–1357, [https://doi.org/10.1016/0016-7037\(90\)90160-M](https://doi.org/10.1016/0016-7037(90)90160-M), 1990.

814 Sharp, Z. D. and Kirschner, D. L.: Quartz-calcite oxygen isotope thermometry: A calibration based on natural isotopic
815 variations, 58, 4491–4501, [https://doi.org/10.1016/0016-7037\(94\)90350-6](https://doi.org/10.1016/0016-7037(94)90350-6), 1994.

816 Skelton, A., Peillod, A., Glodny, J., Klonowska, I., Månbro, C., Lodin, K., and Ring, U.: Preservation of high-P rocks coupled
817 to rock composition and the absence of metamorphic fluids, *Journal of Metamorphic Geology*, 0,
818 <https://doi.org/10.1111/jmg.12466>, 2018.

819 Soukis, K. and Stockli, D. F.: Structural and thermochronometric evidence for multi-stage exhumation of southern Syros,
820 Cycladic islands, Greece, *Tectonophysics*, 595–596, 148–164, <https://doi.org/10.1016/j.tecto.2012.05.017>, 2013.

821 Spear, F. S. and Pattison, D. R. M.: The implications of overstepping for metamorphic assemblage diagrams (MADs), 457,
822 38–46, <https://doi.org/10.1016/j.chemgeo.2017.03.011>, 2017.

823 Spear, F. S. and Selverstone, J.: Quantitative P-T paths from zoned minerals: Theory and tectonic applications, *Contr. Mineral.*
824 *and Petrol.*, 83, 348–357, <https://doi.org/10.1007/BF00371203>, 1983.

825 Spear, F. S., Wark, D. A., Cheney, J. T., Schumacher, J. C., and Watson, E. B.: Zr-in-rutile thermometry in blueschists from
826 Sifnos, Greece, *Contrib Mineral Petrol*, 152, 375–385, <https://doi.org/10.1007/s00410-006-0113-4>, 2006.

827 Syracuse, E. M., van Keken, P. E., and Abers, G. A.: The global range of subduction zone thermal models, *Physics of the Earth
828 and Planetary Interiors*, 183, 73–90, <https://doi.org/10.1016/j.pepi.2010.02.004>, 2010.

829 Thomas, J. B. and Spear, F. S.: Experimental study of quartz inclusions in garnet at pressures up to 3.0 GPa: evaluating validity
830 of the quartz-in-garnet inclusion elastic thermobarometer, *Contrib Mineral Petrol*, 173, 42, <https://doi.org/10.1007/s00410-018-1469-y>, 2018.

832 Tomaschek, F., Kennedy, A. K., Villa, I. M., Lagos, M., and Ballhaus, C.: Zircons from Syros, Cyclades, Greece—
833 Recrystallization and Mobilization of Zircon During High-Pressure Metamorphism, *J Petrology*, 44, 1977–2002,
834 <https://doi.org/10.1093/petrology/egg067>, 2003.

835 Trotet, F., Vidal, O., and Jolivet, L.: Exhumation of Syros and Sifnos metamorphic rocks (Cyclades, Greece). New constraints
836 on the P-T paths, *European Journal of Mineralogy*, 13, 901–902, <https://doi.org/10.1127/0935-1221/2001/0013-0901>, 2001a.

837 Trotet, F., Jolivet, L., and Vidal, O.: Tectono-metamorphic evolution of Syros and Sifnos islands (Cyclades, Greece),
838 *Tectonophysics*, 338, 179–206, [https://doi.org/10.1016/S0040-1951\(01\)00138-X](https://doi.org/10.1016/S0040-1951(01)00138-X), 2001b.

839 Urey, H. C.: The thermodynamic properties of isotopic substances, 562–581, 1947.

840 Uunk, B., Brouwer, F., ter Voorde, M., and Wijbrans, J.: Understanding phengite argon closure using single grain fusion age
841 distributions in the Cycladic Blueschist Unit on Syros, Greece, *Earth and Planetary Science Letters*, 484, 192–203,
842 <https://doi.org/10.1016/j.epsl.2017.12.031>, 2018.

843 Walowski, K. J., Wallace, P. J., Hauri, E. H., Wada, I., and Clynne, M. A.: Slab melting beneath the Cascade Arc driven by
844 dehydration of altered oceanic peridotite, 8, 404–408, <https://doi.org/10.1038/ngeo2417>, 2015.

845 Wang, J., Mao, Z., Jiang, F., and Duffy, T. S.: Elasticity of single-crystal quartz to 10 GPa, *Phys Chem Minerals*, 42, 203–
846 212, <https://doi.org/10.1007/s00269-014-0711-z>, 2015.

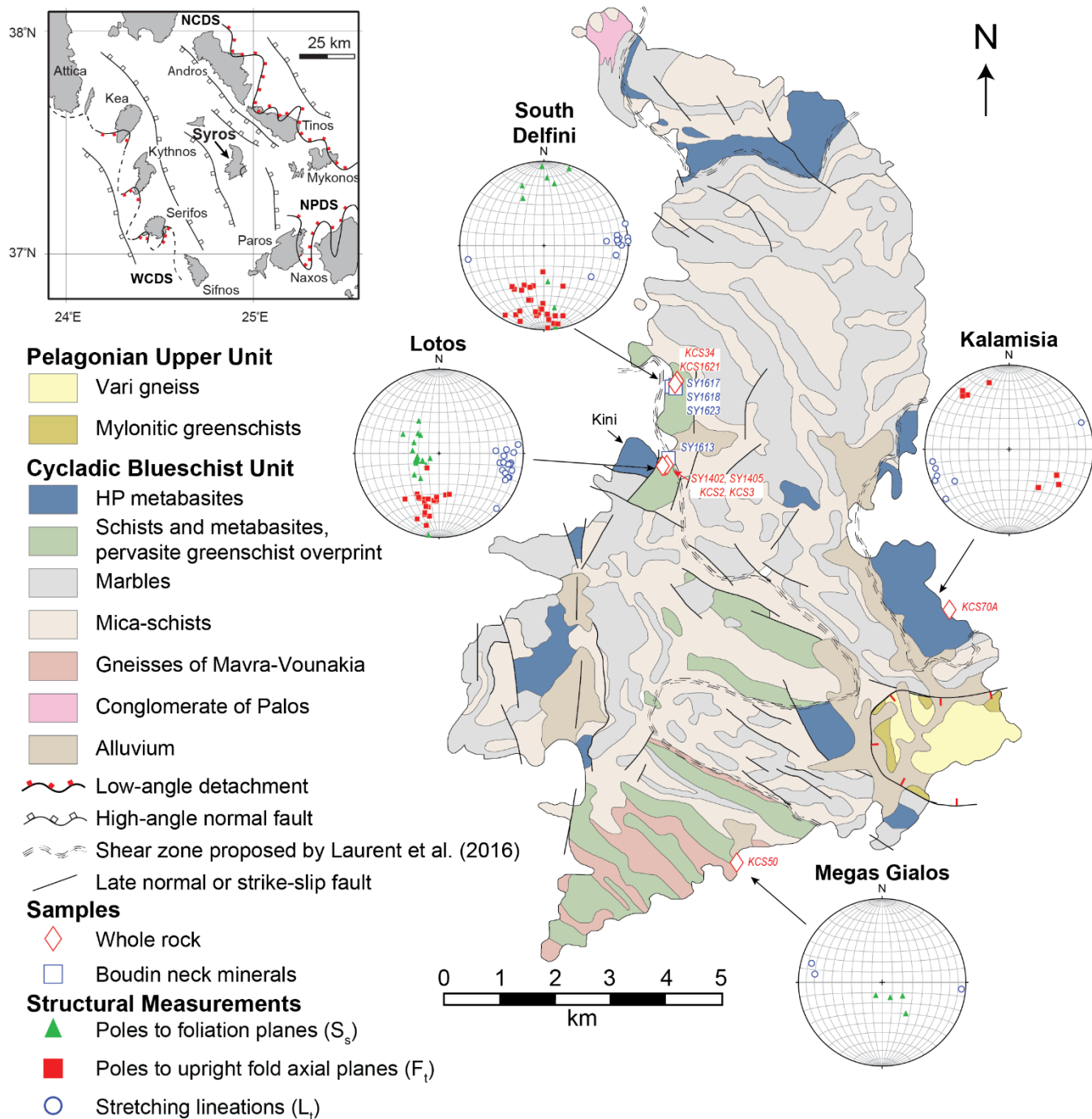
847 Wang, Z. and Ji, S.: Elasticity of six polycrystalline silicate garnets at pressure up to 3.0 GPa, *American Mineralogist*, 86,
848 1209–1218, <https://doi.org/10.2138/am-2001-1009>, 2001.

849 Wunder, B. and Schreyer, W.: Antigorite: High-pressure stability in the system $MgO\text{-}SiO_2\text{-}H_2O$ (MSH), *Lithos*, 41, 213–
850 227, [https://doi.org/10.1016/S0024-4937\(97\)82013-0](https://doi.org/10.1016/S0024-4937(97)82013-0), 1997.

851 Zhang, Y.: Mechanical and phase equilibria in inclusion–host systems, *Earth and Planetary Science Letters*, 157, 209–222,
852 [https://doi.org/10.1016/S0012-821X\(98\)00036-3](https://doi.org/10.1016/S0012-821X(98)00036-3), 1998.

853 Zhong, X., Moulas, E., and Tajčmanová, L.: Post-entrapment modification of residual inclusion pressure and its implications
854 for Raman elastic thermobarometry, 11, 223–240, <https://doi.org/10.5194/se-11-223-2020>, 2020.

855



856

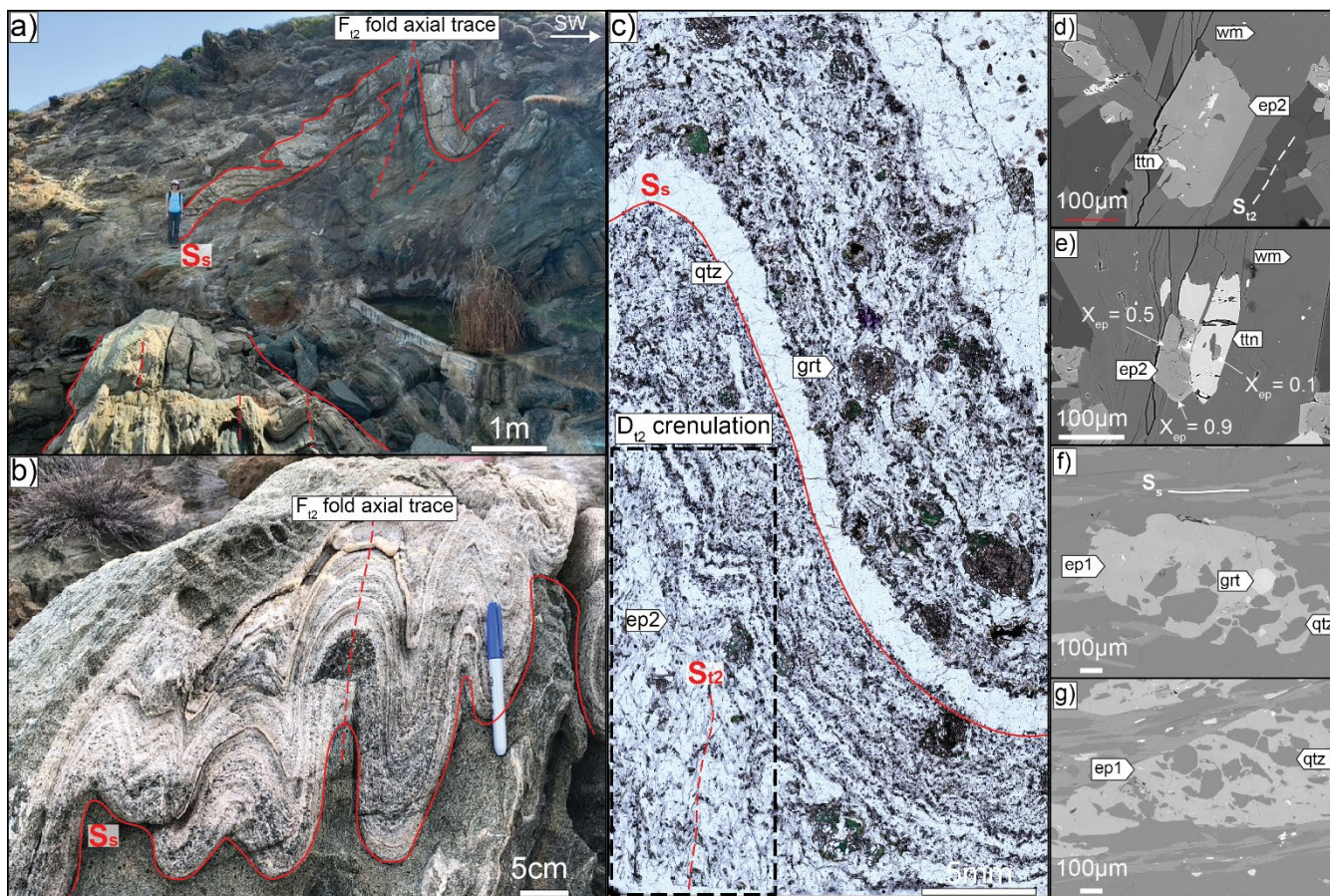
857

858

859

860

Figure 1. Simplified geologic map of Syros, Greece [modified from Keiter et al. (2011)]. Inset map shows Syros relative to the North and West Cycladic, and Naxos-Paros Detachment Systems (NCSD, WCDS, NPDS, modified from Grasemann et al., 2012). Shear zones within the CBU and the Vari detachment are after Laurent et al., 2016 and Soukis and Stockli (2013), respectively. Stereonets from each studied outcrop are shown, and arrows indicate the outcrop location.



862

863 **Figure 2. Outcrop, micrograph, and electron images showing stages of retrograde deformation present in southern Delfini. D_1 and**
 864 **D_{12} represent older and younger stages of deformation, respectively.** a) Upright folds (F_{12}) **formed during D_{12}** , that re-fold the **older**
 865 **primary S_s foliation.** b): Core of F_{12} folds (below Fig. 2a, KCS34). c): Plane light image of sample KCS34; sample cut perpendicular
 866 to the F_{12} fold axial plane. Epidotes (ep2) from the upright fold exhibit recrystallization as indicated by alignment with a late S_{12}
 867 crenulation, and a reduction in inclusions and grain size. d) Ep2 with late titanite (ttn) inclusions. Ep2 is parallel to white mica (wm)
 868 that defines S_{12} (KCS34). e) Ep2 in textural equilibrium with ttn (KCS34). f) Ep1 parallel to S_s , with garnet (grt) and quartz (qtz)
 869 inclusions that do not define an internal foliation (KCS1621). g) Poikiloblastic ep1 parallel to S_s , with a weak internal foliation
 870 defined by qtz (KCS1621).

871

872

873

874

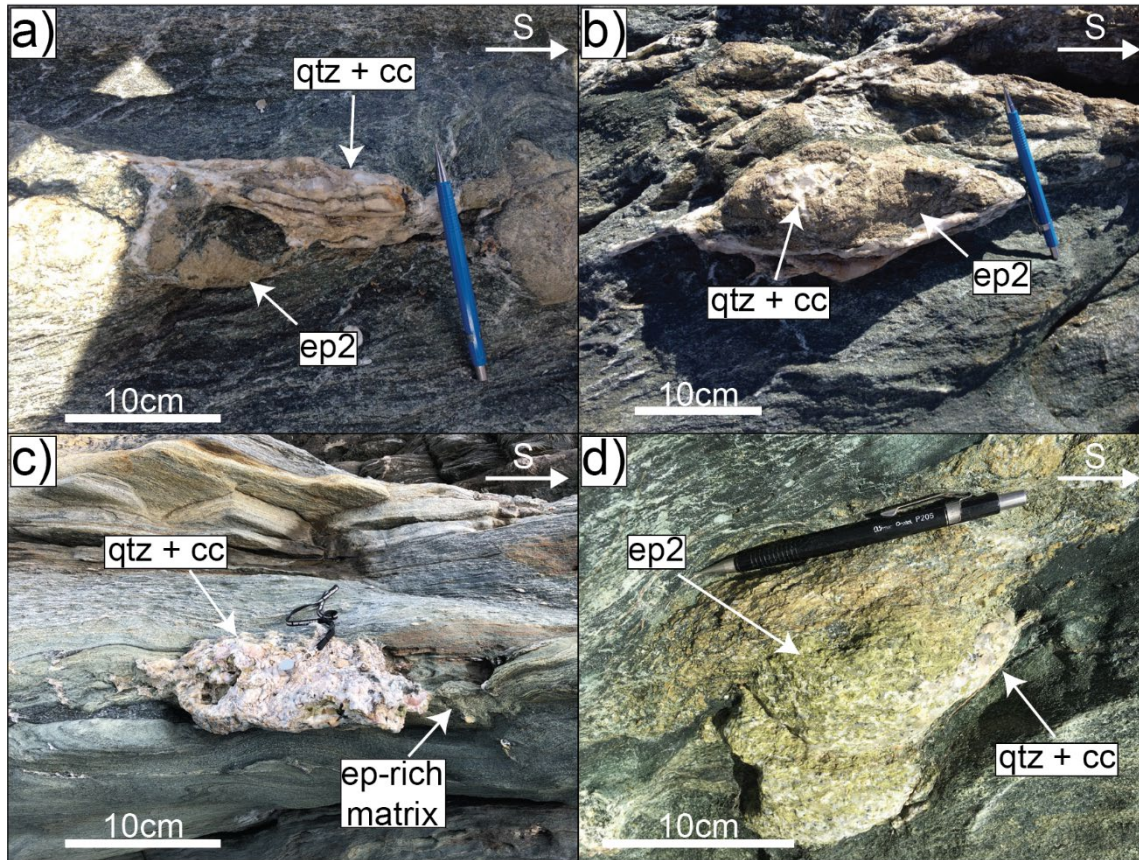
875

876

877

878

879

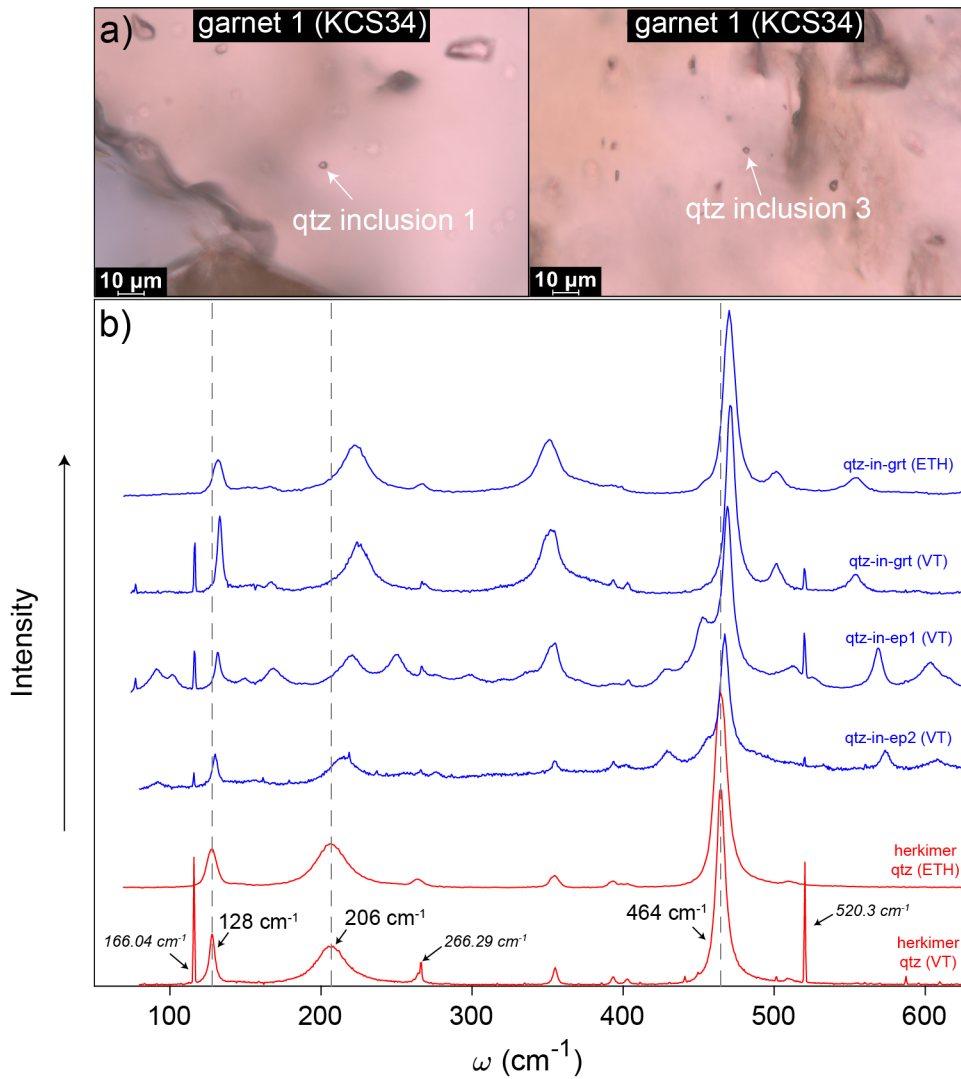


880

881

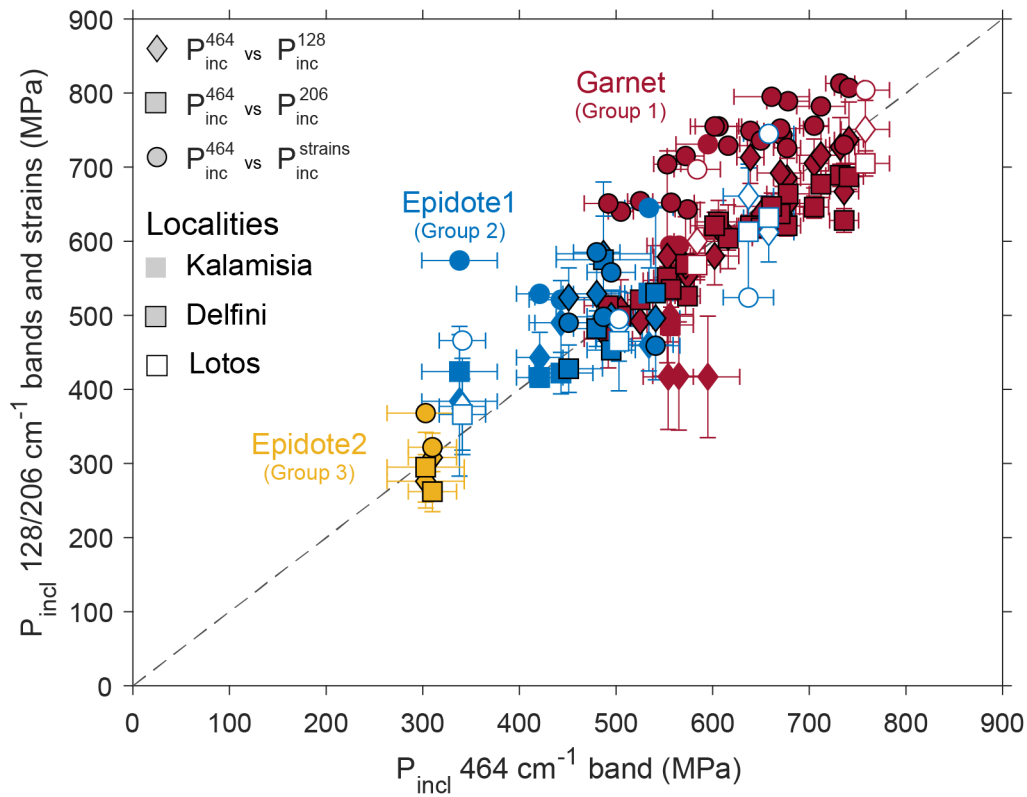
882

Figure 3. Outcrop photos of epidote boudins sampled for oxygen isotope thermometry. a) SY1613 (Lotos), b) SY1617 (Delfini), c) SY1618 (Delfini), d) SY1623 (Delfini). Boudins formed during D₂, parallel to F₂ fold hinge lines.



883

884 **Figure 4. Photomicrographs of measured quartz inclusions in garnet from Delfini (a) and Raman spectrums of unstrained Herkimer**
 885 **quartz and strained quartz inclusions (b). b) Shown for comparison are Herkimer quartz (red) and quartz inclusion (blue)**
 886 **measurements from Virginia Tech and ETH Zürich. Quartz bands and Ar plasma lines (only VT analyses) are numerically labelled.**



887

888 **Figure 5. Comparison of P_{inc} determined from different quartz bands using hydrostatic calibrations, and by using phonon-mode**
 889 **Grüneisen tensors (strains). Red, blue, and yellow symbols indicate qtz-in-grt (Group 1), qtz-in-ep1 (Group 2), and qtz-in-ep2**
 890 **(Group 3) results, respectively. Diamonds, squares, and circles indicate P_{inc}^{464} vs P_{inc}^{128} , P_{inc}^{464} vs P_{inc}^{206} , and P_{inc}^{464} vs $P_{inc}^{strains}$ results,**
 891 **respectively. No border, filled, and open symbols indicate analyses from Kalamisia, Delfini, and Lotos samples, respectively.**

892

893

894

895

896

897

898

899

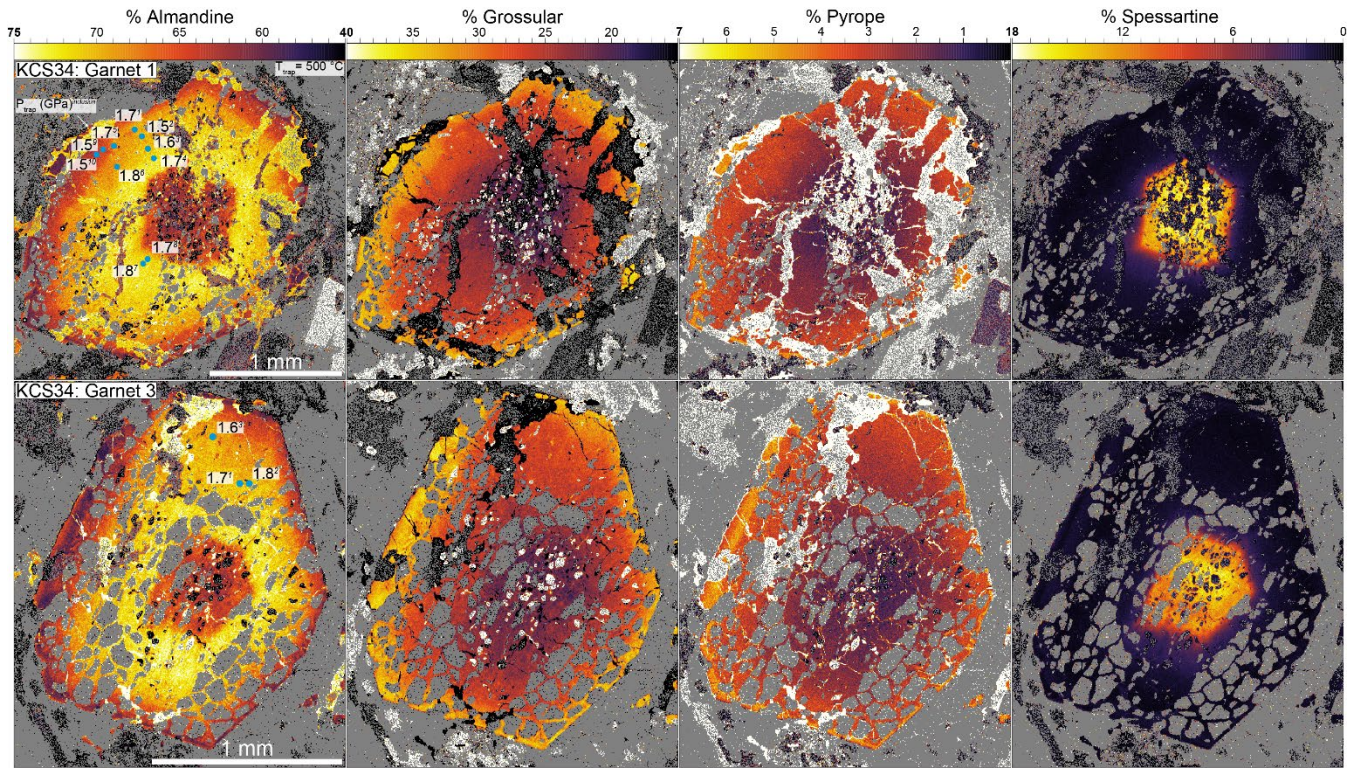
900

901

902

903

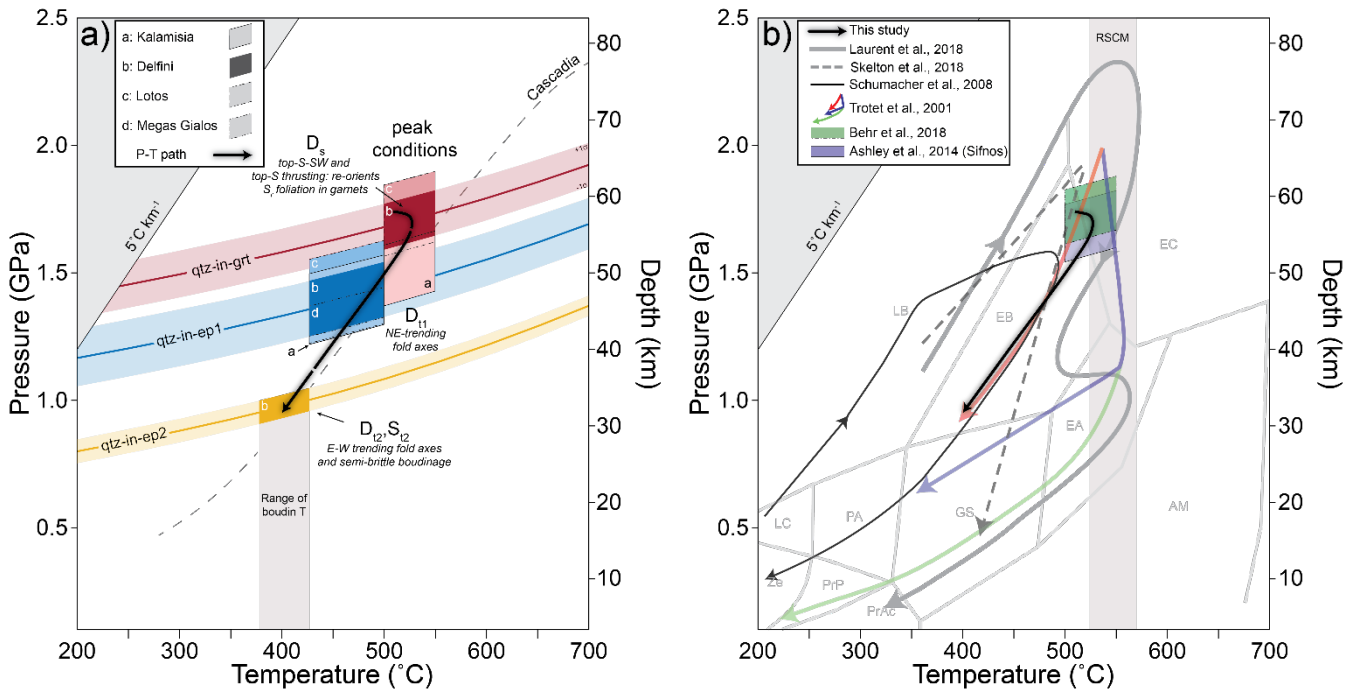
904



905

906 **Figure 6. Compositional x-ray maps of two garnets from sample KCS34 (Delfini). Blue dots indicate the location of measured**
 907 **inclusions; systematic P_{trap} differences are not observed across garnets (P_{trap} units are GPa, calculated at $T_{\text{trap}} = 500$ °C.). Subscripts**
 908 **indicate the inclusion number (see Supplementary Table S3).**

909



910

911 **Figure 7. (a) P-T conditions deduced from elastic thermobarometry and oxygen isotope thermometry superimposed on modeled**
 912 **Cascadia slab-top geotherm (Syracuse et al., 2010) and b) reference P-T conditions. (a) P_{trap} from Groups 1, 2, and 3, that reflect**
 913 **peak (qtz-in-garnet), retrograde blueschist-greenschist facies (qtz-in-ep1, D_{11}), and late greenschist facies (qtz-in-ep2, D_{12})**
 914 **conditions. Solid red, blue, and yellow lines and rectangles are the P_{trap} isomekes (calculated from the mean residual inclusion pressure of each**
 915 **group) and our best-estimate entrapment conditions, respectively. Transparent lines are P_{trap} errors (1σ around the mean)**
 916 **for analyses from Delfini samples. Grey box bounds the range of temperatures calculated from oxygen isotope thermometry of quartz-**
 917 **calcite boudin neck precipitates. D_s is the oldest stage of deformation in outcrop. Subsequent D_i deformation is separated into D_{11}**
 918 **and D_{12} to differentiate older and younger stages of upright folding, respectively, that form NE-SW (D_{11}) and E-W (D_{12})**
 919 **lineations under blueschist and greenschist facies conditions. b) Recalculated P_{trap} values from Behr et al. (2018) (Syros) and Ashley et al.**
 920 **(2014) (Sifnos) and are shown in purple (solid border) and green (dashed border) rectangles, respectively. Metamorphic facies are**
 921 **taken from (Peacock, 1993). Metamorphic facies fields (Peacock, 1993): zeolite (ZE), prehnite-pumpellyite (PrP), prehnite-actinolite**
 922 **(PrAc), pumpellyite-actinolite (PA), lawsonite-chlorite (LC), greenschist (GS), lawsonite-blueschist (LB), epidote-blueschist (EB),**
 923 **epidote-amphibolite (EA), amphibolite (AM), eclogite (EC). RSCM = Raman Spectroscopy of Carbonaceous Material (data from**
 924 **Laurent et al., 2018).**

925

926